remote sensing

MDPI

Article

Environmental Influences on the Detection of Buried Objects with a Ground-Penetrating Radar

Bernd Arendt [1,*], Michael Schneider [1], Winfried Mayer [2] and Thomas Walter [1]

[1] Laboratory of Microtechnology, Institute of Mechatronics and Medical Engineering, University of Applied Science Ulm, 89081 Ulm, Germany; michael.schneider@thu.de (M.S.); thomas.walter@thu.de (T.W.)
[2] FindMine gGmbH, 89257 Illertissen, Germany; winfried.mayer@findmine.org
* Correspondence: bernd.arendt@thu.de

Abstract: A tremendous number of landmines has been buried during the last decade. In recent years, various autonomous platforms equipped with ground-penetrating radars (GPRs) have been proposed for the detection of landmines. These systems have already demonstrated their performance in controlled environments with known ground truth. However, it has been observed that the influence of surface conditions in the form of vegetation and roughness as well as soil moisture content significantly reduce the detection probability. The influence of these individual factors on a ground-offset GPR is presented and discussed in this work. Each of these factors significantly degrades the backscattered signal. With increasing soil moisture, the signal gets attenuated more strongly; however, the signature is maintained in the phase of the C-Scans. An increase in surface roughness deteriorates the target pattern making it difficult to detect buried objects unambiguously. Vegetation, especially with irregular leaf structures, can appear as a ghost target and scatter the electromagnetic waves. In most cases, the target is easier to detect in the phase of the B- or C-Scan.

Keywords: GPR; rough surface; soil moisture content; target pattern; landmines; buried objects; vegetation; SFCW

check for updates

Citation: Arendt, B.; Schneider, M.; Mayer, W.; Walter, T. Environmental Influences on the Detection of Buried Objects with a Ground-Penetrating Radar. *Remote Sens.* **2024**, *16*, 1011. https://doi.org/10.3390/rs16061011

Academic Editor: Lorenzo Capineri

Received: 1 February 2024
Revised: 7 March 2024
Accepted: 11 March 2024
Published: 13 March 2024

1. Introduction

Today the amount of buried landmines has increased tremendously during the last decade. In 2021, 5544 casualties were reported and at least 60 countries are contaminated by antipersonnel mines (APMs). In contrast, only 132.52 km^2 of land has been cleared and become usable for civilians again [1]. This outlines the main problem of humanitarian demining: it is very slow and the goals for mine clearance can not be achieved in an acceptable time period. Therefore, various unmanned aerial vehicles (UAVs) equipped with ground-penetrating radars (GPRs) were proposed to accelerate the process and make the humanitarian demining process safer [2–4]. However, the final testing and confirmation of the system performance in real environments is still pending. Thus, hand-held metal detectors (MDs) or, in individual cases, dual sensors consisting of an MD and a GPR [5,6] are mainly used in humanitarian demining today. Furthermore, there are various approaches for improving the performance of MDs [7].

In particular, for the approaches published in [8,9], which use a GPR on a UAV, the effort for the subsequent processing and focusing of the recorded data is very high. Therefore, these systems are not capable of real-time processing combined with a high degree of hardware complexity, which is a distinct disadvantage in a contaminated mine field. These restrictions become even more stringent due to the fact that the antennas are located at a relatively large distance from the ground surface in contrast to traditional ground-based GPRs. From a safety point of view, ground-based systems cannot be used for mine detection, as there is a risk of unintentional triggering due to the ground pressure or contact with trip wires. Thus, this paper investigates the potential of using a ground-offset GPR at a distance of 30 cm to 50 cm above the ground surface for humanitarian mine detection.

Specifically for subsurface detection, a relatively low frequency is necessary to penetrate into the soil. However, for the above-mentioned small and shallowly buried objects, a large bandwidth with the consequence of a higher center frequency is required. Therefore, various impacts such as the soil moisture content (Section 2.2) can have an impact, causing increased attenuation, reduced transmission power and an enlarged traveling time within the medium. Additionally, an enhanced scattering due to the surface roughness (Section 2.4) leads to a frayed target response as a consequence of multi-path propagation. Vegetation with a high water content (Section 2.3) also results in stronger reflections. These impacts will be discussed in the following, theoretically and on the basis of laboratory measurements.

2. Theory

Prior to the presentation of results, a few radar principles and relations are pointed out, being necessary for the following considerations.

2.1. Radar Principles

With a radar it is possible to measure the distance R and reflectivity of a target. The distance corresponds to the measured time delay τ of the two-way traveled signal to and from a target. Via the received amplitude the radar cross section (RCS) σ of targets can be estimated. Considering an off-ground GPR, it is essential to take into account its interaction with the ground surface. This includes the refraction and reflection of electromagnetic waves at the interface between air and soil. The time traveled in a medium with a higher permittivity ε'_r than the permittivity ε_0 of vacuum is increased due to the reduced propagation velocity of light in a medium c_m:

$$c_\mathrm{m} = \frac{c_0}{\sqrt{\varepsilon_\mathrm{r}\mu_\mathrm{r}}} \tag{1}$$

$$\tau = \frac{2R}{c_m}. \tag{2}$$

Due to refraction, the direction of the propagation of the electromagnetic waves at the interface plane changes. This must be taken into account when observing subsurface objects. According to the Fermat's Principle, the travel time of a electromagnetic wave through a medium is minimized, leading to the following equation:

$$R = \min \| \int n(r)dr \|, \tag{3}$$

including $n(r)$ as the refractive index and dr as the path segment. By fulfilling Fermat's principle, Snell's law of refraction is obtained (Equation (4)), resulting in the typical hyperbolas in the radargram, as illustrated in Figure 1b.

$$\sin(\theta_\mathrm{t}) = \frac{n_1}{n_2}\sin(\theta_\mathrm{i}) \tag{4}$$

$$\cos(\theta_\mathrm{i}) = \frac{\vec{A_1 I_1} \cdot \vec{n}}{\|\vec{A_1 I_1}\| \cdot \|\vec{n}\|} \tag{5}$$

The $\cdot$ denotes the dot product, $\|\vec{A_1 I_1}\|$ the magnitude of the incident vector (c.f. Figure 1a), $\|\vec{n}\|$ the magnitude of the surface normal vector, and θ_i denotes the angle between the incident beam and the surface normal at the intercept I_1, whereas θ_i is the angle between the diffracted beam and the surface normal. The coefficients of reflection R and transmission T can be derived from the Fresnel equations:

$$R_\mathrm{p} = \left| \frac{n_1 \cos(\theta_\mathrm{i}) - n_2 \cos(\theta_t)}{n_1 \cos(\theta_\mathrm{i}) + n_2 \cos(\theta_\mathrm{t})} \right|^2 \quad (6)$$

$$R_\mathrm{s} = \left| \frac{n_1 \cos(\theta_\mathrm{t}) - n_2 \cos(\theta_\mathrm{i})}{n_1 \cos(\theta_\mathrm{t}) + n_2 \cos(\theta_\mathrm{i})} \right|^2 \quad (7)$$

$$T_\mathrm{p} = 1 - R_\mathrm{p} \quad (8)$$

$$T_\mathrm{s} = 1 - R_\mathrm{s} \quad (9)$$

with p representing the parallel and s the perpendicular plane of incidence.

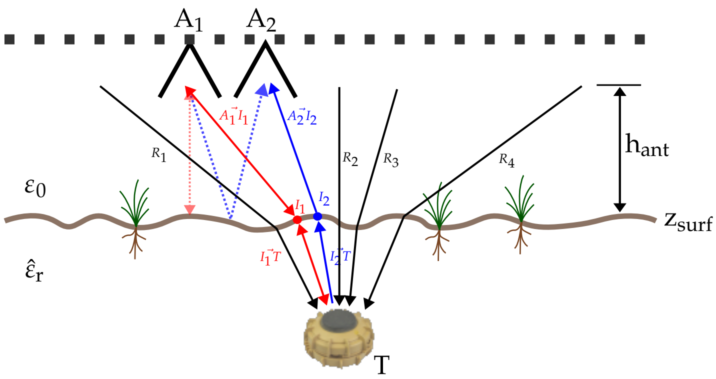

(**a**) Typical of ground-offset GPR scenario

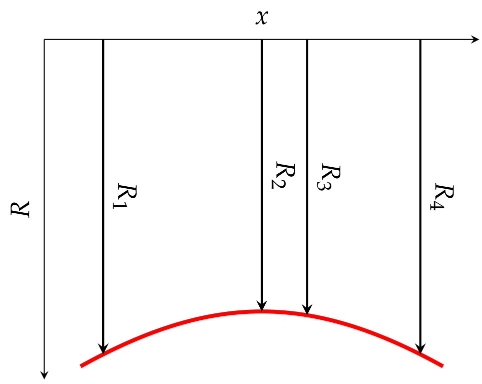

(**b**) Resulting target hyperbola

Figure 1. Sketch of a typical ground-offset GPR scenario in (**a**,**b**) the resulting monostatic target hyperbola (–) due to the increased two-way travel time from a buried target in a B-Scan.

Considering an incidence angle of $\theta_\mathrm{i} = 0^\circ$, R_p becomes equal to R_s. The reflectivity as well as the transmission due to a varying $\hat{\varepsilon}_\mathrm{r}$ for different gravimetric water contents ω_w of the soil are sketched in Figure 2.

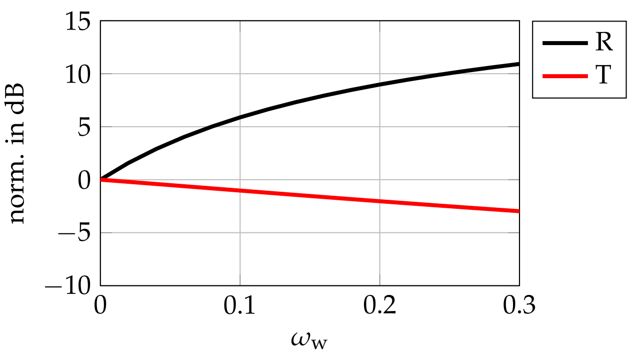

Figure 2. Normalized reflection- and transmission coefficient as a function of gravimetric soil moisture content. Input parameters are center frequency f_c = 2.9 GHz and incident angle $\theta_\mathrm{i} = 0^\circ$.

The terms A-, B- and C-Scan are important for the terminology used in this work. An A-Scan is a single measurement taken at a specific point (■ in Figure 1a) with a time-dependent reflectivity. Multiple A-Scans in a line merge into a B-Scan. Recording several B-Scans, a C-Scan is obtained by slicing the collected data at a certain depth parallel to the surface. As outlined in Figure 1b, there are different principal reflection points. For the monostatic case (–), the transmitting and receiving antenna are collocated (A_1); therefore, the main surface reflection (···) impinges from the area directly under the antenna. The target response in the B-Scan, due to the decreasing and later increasing distance $A_1\vec{I}_1T$, results in a hyperbola with the apex at the actual target position (c.f. Figure 1b).

In contrast to this is the bistatic arrangement with the measured distance being the sum of the two partial distances $A_1\vec{I}_1T$ and $A_2\vec{I}_2T$. The surface reflection also appears in the middle between the antennas ($\cdots$). The apex of the target hyperbola in the bistatic B-Scan is therefore centered between the two antenna positions on either side of the target.

Due to the characteristics of the surface topography, vegetation and soil composition, the target hyperbolas may be deformed and under certain conditions attenuated making it difficult to identify this characteristic pattern in a clutter dominated environment.

Table 1 lists various environmental factors and their related models. In particular, most important is the frequency dependence of water, which has a significant impact on soil and vegetation parameters.

Table 1. Models for various environmental factors.

Environmental Factor	Influence	Model	Comment
water	frequency dependence $\hat{\varepsilon}_r(\omega)$	Debye Model [10] Cole–Cole model [11,12]	basic theory
soil parameters [2]	frequency dependence $\hat{\varepsilon}_r(\omega)$ attenuation α reflection R, transmission T	Peplinski soil model [13] CRIM [1] Topp equation [14]	semi-empirical model for mixed-media empirical model
surface roughness	scattering of EM-waves	Fresnel–Kirchhoff Diffraction [15]	key parameter: σ_h/λ
vegetation [2]	frequency dependence $\hat{\varepsilon}_r(\omega)$ scattering of EM-waves attenuation α	Tan formulation [16] CRIM [1] for homogeneous layer [17]	3D structure/shape not considered

[1] Complex Refractive Index Model; [2] Can be combined with a frequency dependence model for water.

2.1.1. SFCW-Radar

The Stepped Frequency Continues Wave (SFCW) radar modulates the transmit signal in a predefined frequency range with uniform frequency steps Δf. The transmitted frequency f_k of the system is given as:

$$f_k = f_0 + k\Delta f \qquad k = 1, 2, \ldots, K \tag{10}$$

with f_0 being the start frequency and k the number of frequency steps. This generates a bandwidth $B = K\,\Delta f$, which defines also the range resolution δ_R and the theoretical maximum measurement range R_max.

$$\delta_\mathrm{R} = \frac{c_m}{2B} \tag{11}$$

$$R_\mathrm{max} = K \cdot \delta_\mathrm{R} \tag{12}$$

(e.g., with $c_m = c_0$ and $B = 3\,\mathrm{GHz}$ leads to a distance resolution δ_R of 5 cm). The reflected signal $s_k(t)$ from a target at one frequency can be expressed by the amplitude A_k and the time delay τ of the target as:

$$s_k(t) = A_k\,\exp(-j2\pi f_k(t-\tau)). \tag{13}$$

This signal is mixed down to the baseband with a quadratur–demodulator. The output of the quadratur–mixer signals G_k (Equation (14)) yields the target reflectivity over frequency. The output phase $\Phi_k(t)$ (Equation (15)) of the signal can be expressed in terms of the target range R, neglecting the velocity, as discussed in [18]:

$$G_k = A_k \exp(j\Phi_k) \tag{14}$$

$$\Phi_k = -2\pi f_k \frac{2R}{c_m} \tag{15}$$

In order to extract the range information, each burst of k complex samples is Fourier transformed by a Inverse Discrete Fourier Transform (IDFT) to obtain range-delayed reflectivity information. The IDFT is expressed as:

$$H_l = \sum_{k=0}^{K-1} G_k \exp\left(j\left(\frac{2\pi}{K}\right)lk\right) \tag{16}$$

leading to a synthetic range profile that follows a sinc-shaped envelope [18].

2.1.2. SFCW Target Phase

For the results presented later, it is important to estimate the expected phase of the target. For purpose of simplicity, the phase is derived using the continuous inverse Fourier transform. By normalizing the synthetic response with $A_k = 1$ for all k and zero target velocity, the signal only depends on the distance to the target R. Therefore, the phase difference is $\Delta\phi = -4\pi f R/c_m$. Applying the inverse Fourier transform (Equation (17)) leads to:

$$S(t) = \int_{f_c-\frac{B}{2}}^{f_c+\frac{B}{2}} \exp(j\Delta\phi) \cdot \exp(j2\pi f t) df \tag{17}$$

$$= \exp\Bigg(\underbrace{j\,2\pi f_c\left(t - \frac{2R}{c_m}\right)}_{\phi_t}\Bigg) \underbrace{\int_{-\frac{B}{2}}^{\frac{B}{2}} \exp\left(j2\pi f^*\left(t - \frac{2R}{c_m}\right)\right) df^*}_{sinc\left(\pi\left(t-\frac{2R}{c_m}\right)B\right)} \tag{18}$$

with the expected phase ϕ_t of the target as

$$\phi_t = 2\pi f_c\left(t - \frac{2R}{c_m}\right). \tag{19}$$

With $t = 2R/c_m$, the target phase ϕ_t becomes

$$\phi_t = 0 \tag{20}$$

and a sinc-shaped envelope at the target range. This implies that the phase of the target response is always 0 at the correct target distance. Furthermore, the phase along the typical hyperboloid is therefore constant.

2.2. Soil Properties

A radar can sense dielectric contrasts, being the fundamental principle to detect buried objects. Therefore, the properties of the surrounding soil are of great importance. As the radar transmits high-frequency electromagnetic waves, the frequency dependent properties of the soil are of crucial significance. The influences can be divided in two main categories, the velocity of light and the attenuation in the soil. Both factors are strongly dominated by the water content in the soil. The velocity of light in the medium c_m depends on the real part of the permittivity $\hat{\varepsilon}_\mathrm{r}$. Most dry soils exhibit a range of 2.5 to 8 (e.g., dry sand 2.5 to 5), while the real part of water ε_r ranges up ro about 80, explaining the rapid decrease of the velocity of light in the soil with increasing water content [14,19]. The complex permittivity $\hat{\varepsilon}_r$ is given by:

$$\hat{\varepsilon}_\mathrm{r}(\omega) = \varepsilon'_\mathrm{r} + j\varepsilon''_\mathrm{r} \tag{21}$$

with ω the angular frequency. The intrinsic attenuation α in the soil can be calculated with [20]

$$\alpha = 8.686 \cdot \frac{\omega}{c_0} \sqrt{\frac{\varepsilon_\mathrm{r}'(\omega)}{2} \left(\sqrt{1 + \left(\frac{\varepsilon_\mathrm{r}''(\omega)}{\varepsilon_\mathrm{r}'(\omega)} \right)^2} + 1 \right)}. \tag{22}$$

For the soil, it is crucial to look at the resonance frequency of water in the range of 10 GHz to 11 GHz. In this range, the imaginary part (ε_r'') of water increases and therefore the attenuation becomes significantly stronger. The frequency dependence $\hat{\varepsilon}_\mathrm{r}(\omega)$ of water can be expressed by the Debye's formula [10]:

$$\hat{\varepsilon}_\mathrm{r}(\omega) = \varepsilon_\mathrm{r}(\infty) + \frac{\varepsilon_\mathrm{r}(0) - \varepsilon_r(\infty)}{1 + j\omega\tau_\mathrm{r}} \tag{23}$$

with the pole relaxation time τ_r. (The Debye relaxation time specifies the time required of the polarization response to reach about 63 % of its steady-state value when exposed to an external electric field.) Accepted parameters are $\tau_\mathrm{r} \approx 9.231$ ps, $\varepsilon_\mathrm{r}(0) \approx 80$ and $\varepsilon_\mathrm{r}(\infty) \approx 4.5$ [21]. The frequency dependency for these specific values is illustrated in Figure 3.

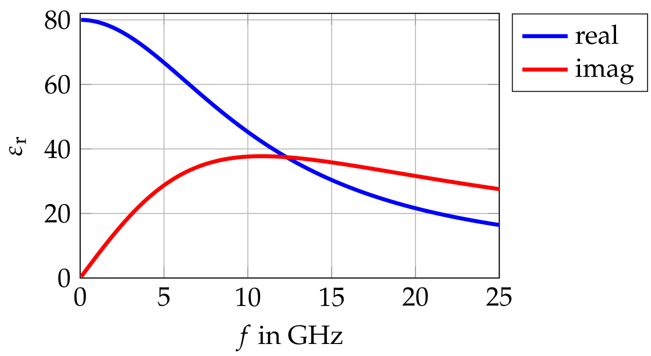

Figure 3. Frequency dependency of $\hat{\varepsilon}_\mathrm{r}$ in water according to the Debye model (Equation (23)).

Another model published by Topp [14] concerning the volumetric water content θ_w and the resulting ε_r of the soil leads to the following relation:

$$\varepsilon_\mathrm{r}{}' = 3.03 + 9.3\theta_\mathrm{w} + 146\theta_\mathrm{w}^2 + 76.7\theta_\mathrm{w}^3 \tag{24}$$

The composition or bulk density of the respective soil is not taken into account here, which can lead to a variation of ε'_r (details can be found in [22,23]). Additionally, the model assumes, that the ε_r' of the dry soil is always 3.03. In addition, it is easier to determine the gravimetric water content ω_w in the field, making it necessary to convert the gravimetric water content ω_w into the volumetric water content θ_w. This requires the bulk density ρ of the soil and leads to $\theta_\mathrm{w} = \omega_\mathrm{w}\rho$.

Considering these aspects, it is more expedient to look at a Complex Refractive Index Model (CRIM), which includes both the air content and the other constituents of the soil [13]. An illustrative formulation of the model would be:

$$\hat{\varepsilon}_r = \left(\theta_\mathrm{air}\, \varepsilon_\mathrm{r,\,air}^\beta + \theta_\mathrm{soil}\, \varepsilon_\mathrm{r,\,soil}^\beta + \theta_\mathrm{water}\, \varepsilon_\mathrm{r,\,water}^\beta(f)\right)^{\frac{1}{\beta}}, \tag{25}$$

with $\beta = 0.5$. Combining the Debye model for the frequency dependency of water with the CRIM model results in a typical representation of the $\hat{\varepsilon}_r$ of the soil, see Figure 4. Furthermore, the attenuation α can be determined via Equation (22), which is illustrated in Figure 4c.

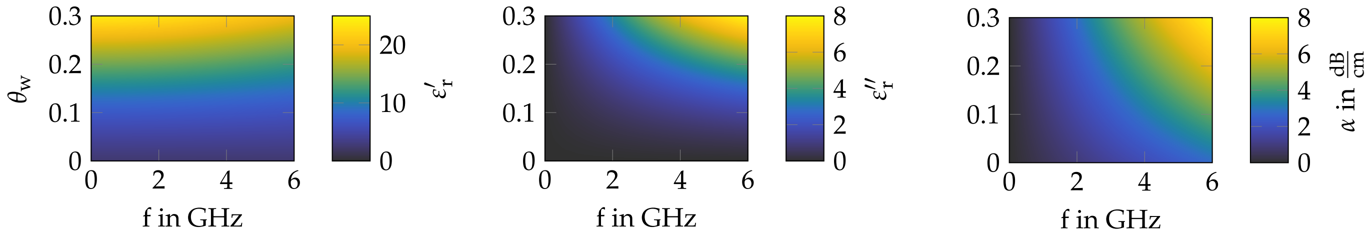

(**a**) Real part of soils $\hat{\varepsilon}_\mathrm{r}$ (**b**) Imaginary part of soils $\hat{\varepsilon}_\mathrm{r}$ (**c**) Attenuation α of the soil

Figure 4. Frequency and water content dependent soil properties, calculated from the CRIM model (Equation (25)) combined with the Debye formulation (Equation (23)) for $\varepsilon_{\mathrm{r,\,soil}} = 2.5$ and $\beta = 0.5$.

Clearly, it can be derived that the real part rises sharply as the water content increases. The imaginary part increases at a higher frequency and a larger water content. The attenuation of the soil behaves in an equivalent way.

2.3. Vegetation

Plants can also play a decisive role for the detection of small buried objects. Tan examined in [16] various plants with respect to their permittivity at a frequency of 9.5 GHz and found the following formulation

$$\hat{\varepsilon}_{\mathrm{r,\,veg}} = 1.5 + \left(\frac{\varepsilon'_{\mathrm{r,w}}(\omega)}{2} - j\frac{\varepsilon''_{\mathrm{r,w}}(\omega)}{3} \right)\omega_\mathrm{w} \tag{26}$$

with $\varepsilon'_{\mathrm{r,w}}(\omega)$ and $\varepsilon''_{\mathrm{r,w}}(\omega)$ being the real and imaginary part of $\hat{\varepsilon}_\mathrm{r}(\omega)$ for water and the gravimetric water content ω_w, while the 1.5 represents the ε'_r of dry vegetation. The observed dependency of the water content is similar to the one in soil. However, it is not the attenuation that is the critical factor here, but rather the scattering that occurs due to the high ε'_r, interfering with the target signal [24], as growing plants posess in particular a high water content.

2.4. Surface Roughness

When an electromagnetic wave passes from one medium to another, the surface roughness may lead to scattering. Scattering occurs when the reflected wave front is deformed so that it propagates in different directions without having a preferred direction. The polarization of the electromagnetic waves can also be affected. Thereby, the scattering is a function of the incidence angle θ_i and the size of the surface elements (roughness). If a surface is specular, nearly no scattering appears. In contrast, with increasing surface roughness and incidence angle the scattering increases and becomes diffuse for a completely rough surface. This scattering depends on the relationship between the wavelength λ of the electromagnetic wave and the standard height deviation σ_h of the surface roughness [15]. Whether a surface is rough or not, is defined by two criteria:

1. Rayleigh Criterion:

$$\sigma_h < \frac{\lambda}{8\ \cos(\theta_i)} \tag{27}$$

2. Fraunhofer Criterion:

$$\sigma_h < \frac{\lambda}{32\ \cos(\theta_i)} \tag{28}$$

The Fraunhofer criterion can be applied in order to decide whether a surface can be considered as rough. For this limit, the phase error remains smaller than pi/8 [25].

The theoretical height function z of a random rough surface is given by the folloing:

$$z = \xi(x, y) \tag{29}$$

The surface height distribution, being considered in this context, is statistically described by a Gaussian distribution, which is valid for a wide range of surfaces [26]. The height probability distribution defines the height deviation from a mean reference plane. Hereafter, the $\langle \xi(x,y) \rangle = z_{\mathrm{surf}}$ is the base for the following discussions and diagrams [27]. The Gaussian height probability is

$$\rho_h(\xi) = \frac{1}{\sigma_h \sqrt{2\pi}} \exp\left(-\frac{\xi^2}{2\sigma^2}\right), \tag{30}$$

with σ_h being the root mean square (RMS) height, which is equal to the standard height deviation. The distribution along the surface of the height profile can be described by the autocorrelation function

$$C(x,y) = \exp\left(-\frac{x^2}{\ell_x} - \frac{y^2}{\ell_y}\right), \tag{31}$$

where ℓ_x and ℓ_y are the correlation lengths in $x-$ and $y-$direction. For the following discussions we assume that the surfaces are isotropic and therefore $\ell_x = \ell_y$. This means that the slope distributions will also be Gaussian. For the isotropic case, the RMS slopes w in x and y are identical and given by Equation (32) [28].

$$w = \sqrt{2}\,\frac{\sigma_h}{\ell} \tag{32}$$

For reference measurements in the laboratory, the three-dimensional rough surfaces were synthesized by a fast convolution and are defined by

$$\xi(x,y) = \mathcal{F}^{-1}\Big(\mathcal{F}\big(n(x,y)\big) \cdot \mathcal{F}\big(C(x,y)\big)\Big) \tag{33}$$

as discussed in [15], with $n(x,y)$ being white noise, which is multiplied in the frequency domain by the correlation kernel $C(x,y)$ and afterwards transformed back into the spatial domain. These synthesized rough surfaces with defined correlation lengths ℓ_x, ℓ_y and standard height deviation σ_h were 3D-printed and used as molds, illustrated in Figure 5, to generate rough soil surfaces.

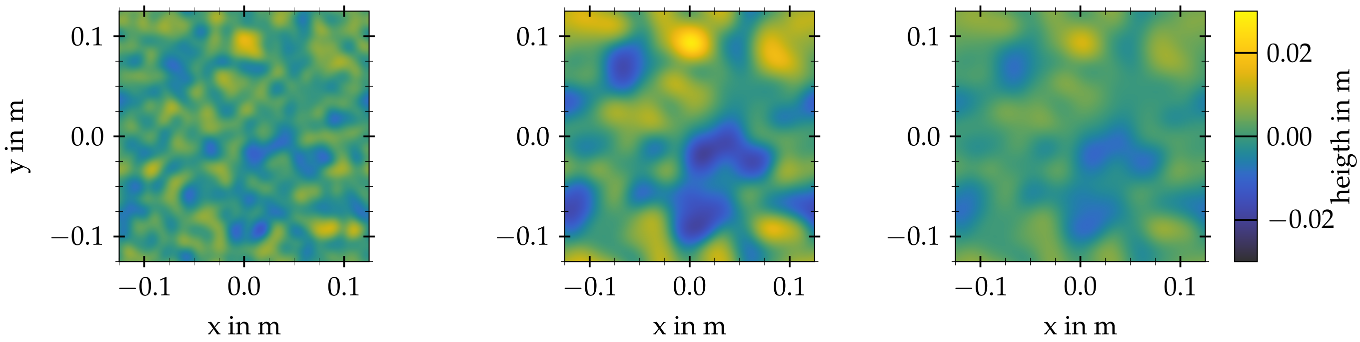

(**a**) surface 1 (**b**) surface 2 (**c**) surface 3

Figure 5. Height map of three different 3D-printed surface molds, with a edge length of 0.25 m and different correlation lengths ℓ and height deviation σ_h, compared in Table 2.

Table 2. Parameters of the synthetically generated rough surfaces.

Parameter	Surface 1	Surface 2	Surface 3
edge length	0.25 m	0.25 m	0.25 m
ℓ	26.25 mm	26.25 mm	13.125 mm
σ_h	3.75 mm	7.5 mm	3.75 mm
ω	0.202	0.404	0.404

2.5. Laboratory Measurements

2.5.1. Setup

Due to the given application of landmine detection, a GPR is investigated with the antennas guided at a fixed distance d_{ant} = 0.28 m between the transmitter A_1 and receiver A_2 and a defined distance h_{ant} = 0.3 m to the ground surface. To record a C-Scan, the soil box (Figure 6b) is scanned with an equidistant grid of Δx and Δy of 0.03 m. A C-Scan therefore consists of $n \times m$ data points, which are picked from the corresponding range bin of the individual A-Scans, resulting in a slice parallel to the surface (xy-plane). While a B-Scan parallel to the y-axis consists of m A-Scans and covers a length of $m \cdot \Delta y$ with $m = 0, 1, 2, \ldots, M$, (the same is valid for a B-Scan parallel to the x-Axis, see Figure 7). The Vector Network Analyzer (VNA) (Keysight handheld VNA [29]) measures a defined frequency range at each position $P(x, y)$. Horn antennas from Aaronia [30] have been mounted. Table 3 gives an overview of the parameters.

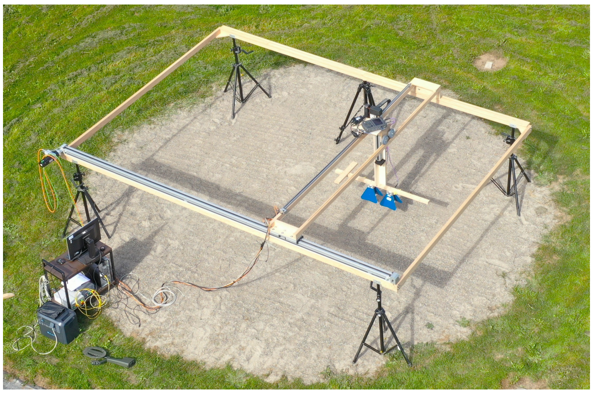

(**a**) field measurements

(**b**) scanning surface 3

Figure 6. Linear Rail System during field measurements (**a**) with the same setup as in the laboratory (**b**).

Table 3. Laboratory setup parameters.

Parameter	Value	Comment
VNA Frequency Range	0.8 GHz to 5 GHz	1001 points
width of range bin ΔR_{bin}	4.4 mm	zero padding of 8
Antenna Bandwidth	0.7 GHz to 18 GHz	Double Ridge Horn [30]
Antenna Beamwidth	≈80° to 30°	-
Δx, Δy	0.03 m	-
h_{ant}	0.3 m	-
d_{ant}	0.28 m	-
soil type	loamy sand	-

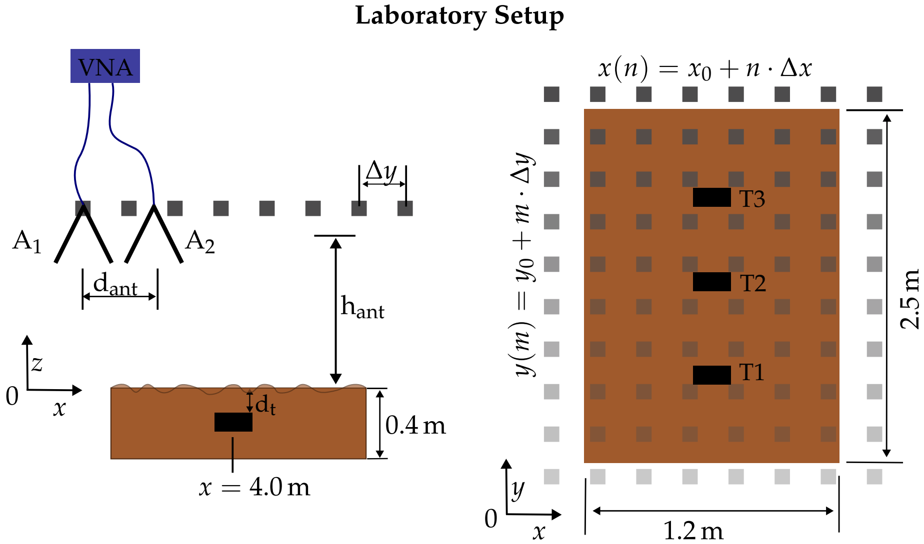

Figure 7. Sketch of the laboratory setup with the symbols used.

Loamy sand is taken as the test soil, making it possible to mold the rough surface (Section 2.5.3). Furthermore, this type of soil can store more water than to pure sand, but less than clayey soil. In addition, grass and other plants can be grown easily (Section 2.5.4).

2.5.2. Buried Test Objects

Two different types of targets have been used for the laboratory measurements. These objects correspond to the size of an APM, see Figure 8. The aluminum cylinder (a) represents a strong and therefore an easily to detect object and is well suited as reference object. In contrast, the plastic cylinder (b) has a smaller RCS and is therefore a very challenging target. These APM simulants are usually buried at 2 cm to 5 cm.

In the laboratory setting, the APM simulants were buried in three positions (T1 (4.0, 1.0), T2 (4.0, 1.62) and T3 (4.0, 2.2) in Figure 7), ensuring sufficient spacing around to prevent mutual interference. Additionally, the simulants were also placed in varying depths, facilitating a comprehensive analysis of the impact of the burial depth on the detectability.

(**a**) Aluminum cylinder (**b**) Plastic cylinder

Figure 8. Buried test objects in the laboratory. The red coin with a diameter of 3 cm can be used as a reference. The aluminum cylinder in (**a**) and the plastic cylinder in (**b**) have a outer diameter of 0.08 m and a height of 0.04 m.

2.5.3. Rough Surface

Rough surfaces can lower the detection capability drastically. Therefore, the synthetically generated surfaces as described in Section 2.4 were 3D printed and used as a mold for the soil surface, parameters in Table 2. Due to the limited print volume, the three different surfaces, each with an edge length of 0.25 m, were placed next to each other to generate a structure on the entire surface. For this reason, the structure is repeated periodically, see Figure 9.

(**a**) Periodically repeated pattern (**b**) Zoomed in section

Figure 9. Example image of Surface 2, showing the periodicity (**a**) and a zoomed in section (**b**).

For the frequency range of 0.8 GHz to 5 GHz used in the measurements, the limits for the standard height deviation, whether a surface is considered as rough or not, are calculated for the Fraunhofer and Rayleigh criteria, shown in Table 4. Based on the limits of the Fraunhofer criterion Equation (28) compared to σ_h of the synthetically generated surfaces in Table 2, the surfaces used are categorized as rough in the upper frequency range, while none of the surfaces are classified as rough for the starting frequency.

Table 4. Rough surface criteria.

Wavelength	Rayleigh Criterion	Fraunhofer Criterion
$\lambda_{\text{max}} = 0.37\,\text{m}$	46.25 mm	11.56 mm
$\lambda_{\text{c}} = 0.10\,\text{m}$	12.87 mm	3.22 mm
$\lambda_{\text{min}} = 0.06\,\text{m}$	7.5 mm	1.87 mm

2.5.4. Vegetation

The plants shown in Figure 10 were grown in the laboratory. They differ in their structure and the water content of the individual leaf segments. The grass with a height of 0.1 m (a) has an uniform distribution over the entire test area. The coltsfoot (c), on the other hand, has larger leaves on individual stems with a higher water content, as well as a stronger root system that forms branches. In contrast, the thistle (b) rises from a central root, which also penetrates deep into the soil. The thistle also contains a lot of water in its stems during growth, which is no longer present to the same extent in summer and fall.

(**a**) (**b**) (**c**)

Figure 10. Vegetation grown in the laboratory. (**a**) grass (lat. *lolium perenne esquire*), (**b**) thistle (lat. *carduus nutans*), (**c**) coltsfoot (lat. *tussilago farfara*).

2.6. SFCW GPR Data Processing

The processing of the data is straightforward and is basically based on the steps listed in Figure 11. The S-parameters, s_{11} and s_{21}, are recorded with the VNA at each approached position. This allows monostatic measurements s_{11}, with antenna A1, and bistatic measurements s_{21}, with antenna A_1 as transmitter and A_2 as receiver. These are now combined with the corresponding antenna position $\vec{P}_{\text{ant}}$ of the two antennas A_1 and A_2. The data are then transformed into the time domain using the inverse IDFT to obtain the reflectivity over distance, Equation (16). Data are windowed with a Hanning window to reduce the sidelobes [31,32]. The signal is zero-padded to the next power of two and then oversampled eight times. This leads to a range bin resolution $\Delta R_{\text{bin}} = \delta_{\text{R}} K / N_{\text{idft}}$ of rounded 4.4 mm for the results presented in the following. The next step, distance correction, is particularly important with respect to the following evaluation of the surface and the target response. Thus, the cable length is compensated up to the phase center of the antenna so that the surface appears at the correct distance [33].

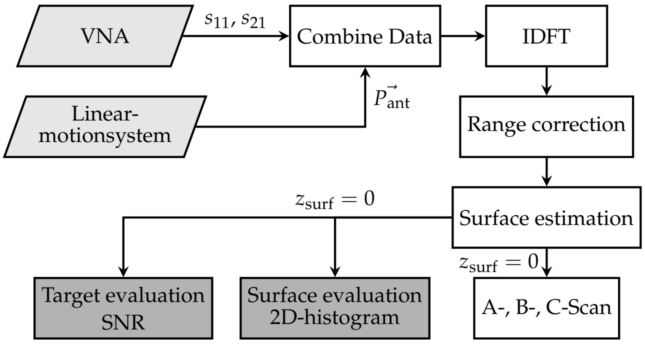

Figure 11. Overview of data processing.

The imaging is based on a narrow measurement grid, and no migration algorithm or focusing was applied. To generate a C-Scan, the data point corresponding to a specific depth is picked from each A-Scan, which is equivalent to a slice parallel to the surface. These data points are displayed for the power C-Scan using an interpolating shader. For the phase C-Scans, the respective phase at the data point is displayed without interpolation to avoid discontinuities caused by the wrapped phase. The B-scans are presented using the equivalent scheme.

2.6.1. Surface Evaluation

Following these steps, the final surface position is estimated in the data by searching for the first dominant peak in the range data of each A-Scan. Based on this, the A-, B- and C-Scans are extracted and displayed. The different targets and the characteristics of the surface are also evaluated based on this concept. In order to determine the influence of various rough surfaces and vegetation on the surface signal, various parameter distributions are determined from the images. First, the distribution of the maximum response over the entire surface is determined, resulting in two parameters. Firstly, the distribution of the signal strength and secondly the position of the peak, from which a bivariate histogram with the distribution of the signal strength over the position can then be created. This can be used to evaluate and compare the influence of the respective surface under investigation.

2.6.2. Target Evaluation

For the target evaluation the signal-to-noise ratio (SNR) is determined for the targets in the individual experiments. In general, the SNR measures the intensity of the signal power P_{Signal} in comparison to the background noise or clutter $P_{\text{Background}}$. It is expressed as:

$$SNR = \frac{P_{\text{Signal}}}{P_{\text{Background}}}. \tag{34}$$

2.7. Determination of Environmental Parameters

Determination of separate environmental parameters is of major importance, particularly the gravimetric water content ω_{w} of the soil and vegetation. Additionally, the vegetation density d_{v} (in mass per unit area) and height h_v represent key parameters. The

3D-structure of individual plants varies depending on the species and cannot be described by a simple model. Surfaces with defined roughness parameters are synthesized by a molding technique, characterized by correlation length ℓ and standard height deviation σ_h as listed in Table 2. Table 5 provides an overview of the considered parameters.

Table 5. Environmental parameters.

Parameter	Formula	Unit	Comment
gravimetric soil moisture content	$\omega_\mathrm{W} = \frac{m_\mathrm{w} - m_\mathrm{d}}{m_\mathrm{d}}$	$[\%]$	ISO 11465 dryed at110 °C
surface roughness	parameters Table 2, criteria in Table 4		molds are synthetically generated
vegtation mass per area	$d_\mathrm{v} = \frac{m_\mathrm{v}}{A}$	$\left[\frac{\mathrm{kg}}{\mathrm{m}^2}\right]$	-
gravimetric vegetation moisture content	$\omega_\mathrm{W} = \frac{m_\mathrm{w} - m_\mathrm{d}}{m_\mathrm{d}}$	$[\%]$	dryed at 110 °C
vegetation height	h_v	$[\mathrm{m}]$	-
vegetation structure	-		different for each plant species

3. Results

The measurements recorded in the laboratory will be presented and discussed in the following chapters. The influence of the soil moisture content is evaluated first, followed by the surface roughness and the vegetation. In the B-Scans, the y-target positions are marked with a ( ) at the bottom.

3.1. *Influence of the Soil Moisture*

In the following, the influence of the gravimetric soil water content will be evaluated. An increased travel time in the medium combined with a stronger surface reflection, as a result of an increased ε_r' can be predicted. This leads to the consequence that less power penetrates the ground and that the surface reflection dominates the target response of shallowly buried targets. Furthermore, attenuation α increases based on the ε_r'' rise, resulting in an attenuated signal for deeper targets.

Soil samples were taken during the individual measurements and used to determine the gravimetric soil moisture content ω_W. The ε_r' was determined from the distance between the soil surface and the target in the A-Scan centered above the target. The results are given in Figure 12. The investigated gravimetric soil moisture content ω_W of 0.012 to 0.1 leads to a variation of ε_r' from 2.5 to 8.4. In this range, the relationship can be assumed to be linear. Deviations can be attributed to measurement tolerances of the weight, as well as to an eventually inhomogeneous moisture distribution within the soil. For the presented observations, the accuracy is still sufficient and matches well to the theory, c.f. Figure 4a.

Looking at the B-Scans with different soil moisture contents in Figure 13, it can be observed that the surface reflectance increases with the soil moisture content, varying from −60 dB for the dry soil up to an increased response of −54 dB for a gravimetric soil moisture content of 0.1, which is a rise of 6 dB, being in the range predicted by theory, c.f. Figure 2. A more detailed analysis is presented in Figure 14 for three different soil moisture contents. In the histograms the probability density function (pdf) for the power over position distribution is given. In the surface position a small variation is visible, which is caused by a not perfect smooth surface. The main focus here should be put on the power distribution, which in all three cases is approximately 3dB wide for the majority of the reflected power. The average value increases with increasing soil moisture content. This relationship is given for other moisture contents in Figure 15a (•) and behaves accordingly.

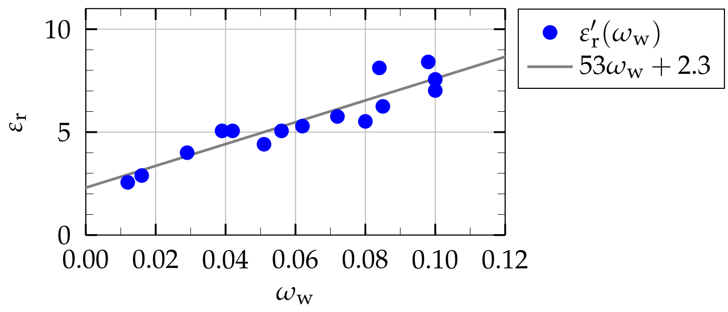

Figure 12. ε_r' dependency on the gravimetric soil moisture content ω_w of sandy loam, measured with a center frequency f_c of 2.9 GHz.

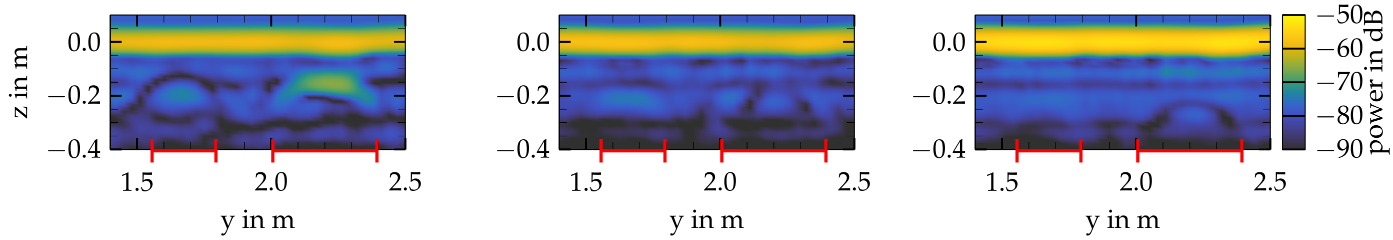

(**a**) $\omega_w = 0.012$ (**b**) $\omega_w = 0.042$ (**c**) $\omega_w = 0.1$

Figure 13. B-Scans at x = 4.00 with different soil moisture content from a buried aluminum cylinder (Figure 8a) at (4.00, 2.20, −0.1) and a plastic cylinder (Figure 8b) at (4.00, 1.65, −0.1).

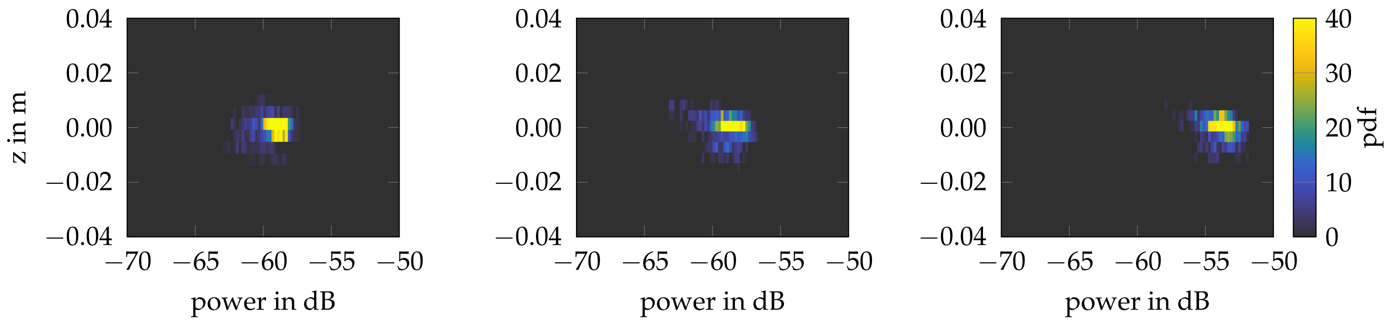

(**a**) $\omega_w = 0.012$ (**b**) $\omega_w = 0.051$ (**c**) $\omega_w = 0.098$

Figure 14. Surface power vs. position distribution histograms for different soil moisture contents illustrating the dependency of the mean surface response from the soil moisture content without a wide spreading in position.

Another observation in the B-Scans implies that the clutter pattern is the same for all B-Scans, leading to the assumption that this is not directly influenced by the humidity and is rather dominated by the experimental setup, e.g., the antenna ringing. However, as a consequence this leads to the superposition of the target signal with a varying background signal level.

The buried aluminum cylinder at (4.00, 2.20, −0.1) is visible in all B-Scans (Figure 13) with a decreasing intensity. Especially in the B-Scan with the highest soil moisture content, it is only recognizable due to the hyperbolic negative contrast pattern, as the signal level is in the range of the background level.

In Figure 15a the reflected power from the target is displayed (•) depending on the soil moisture content. The graph implies a falling curve for an increasing moisture content. However, there is a slight increase in the target response for a water content of 0.08, which is due to a constructive interference with the previously described clutter.

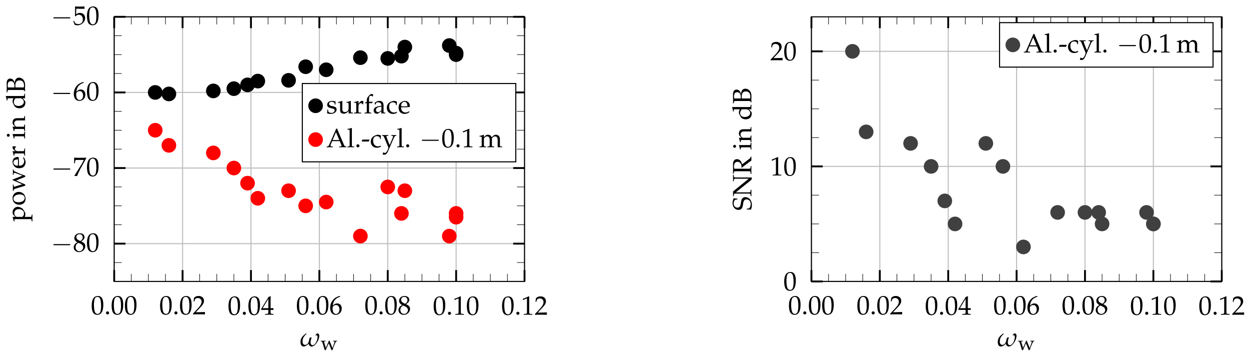

(**a**) target and surface reflected power (**b**) SNR of a buried aluminum cylinder

Figure 15. Reflected power and SNR of sandy loam against the gravimetric soil moisture content ω_w, measured at a center frequency f_c of 2.9 GHz.

For further analysis, the SNR in Figure 15b is taken into consideration. The influence of the background noise is even more apparent. As the object response appears deeper (c.f. Figure 13), due to the increased ε_r', the response is superimposed with another part of the "static" clutter. Therefore, the phase progression of the clutter is also important for the target response. As an example, two points will be analyzed in more detail, the first for a soil with ω_w = 0.012 and the second with 0.062. For the dryer soil, the target range coincides with a minimum of the clutter and resulting in a high SNR of 20 dB, c.f. Figure 15b. On the other hand, for an increased soil moisture content, the target response is reduced. Additionally, for ω_w = 0.062, the target response coincides with a local maximum of the clutter and results in a very low SNR of 3 dB, which is not sufficient to detect a target in a B-Scan without the occurrence of negative contrast hyperbola.

Taking a closer look at the buried plastic cylinder, it is only detectable in the two B-Scans of the dryer soil, Figure 13a,b.

In Figure 16, B-Scans of a shallowly (d_t = 0.03 cm) buried aluminum cylinder are shown. The surface reflection increases to the same level as described before. In the dry soil, the shallowly buried aluminum cylinder is recognizable, but the typical hyperbola are not clearly visible due to the insufficient distance resolution δ_R. This behavior is also clearly observable in the corresponding A-Scan in Figure 17a (–). The target only forms a saddle point in the declining surface response. If the traveled time in the soil is increased as a result of the higher ε_r', the target becomes more distinctly visible, c.f. Figure 13b. The separation between the surface and the target response clearly appears in the A-Scan (–). Another important point to be noted is that the surface response directly above the target is reduced based on the complex interference, which leads to a constructive or destructive superposition. With further increase of the soil moisture, the buried object is no longer visible due to the increased surface reflection. However, if we compare the surface peak of the presented A-Scans (–) for the soil moisture content ω_w = 0.051, it becomes obvious that the surface response directly above the shallowly buried aluminum cylinder is reduced by 3 dB in comparison to the other A-Scans. A more detailed analysis will be discussed later.

In the A-Scans, the afore-mentioned clutter pattern is also apparent. For the aluminum cylinder buried at −0.1 m the influence of the ε_r' and the resulting elongation, as well as the attenuation due to the increasing ε_r'', is obvious.

With respect to the clutter pattern and the resulting SNR, detection based on A- and B-Scans appears very difficult. In particular, the appearance of a hyperbola in the B-Scan is strongly influenced by the clutter level, which varies due to the increased travel time in the medium. However, a C-Scan can be created on the basis of a further measurement dimension which can be used for further evaluation to detect these objects.

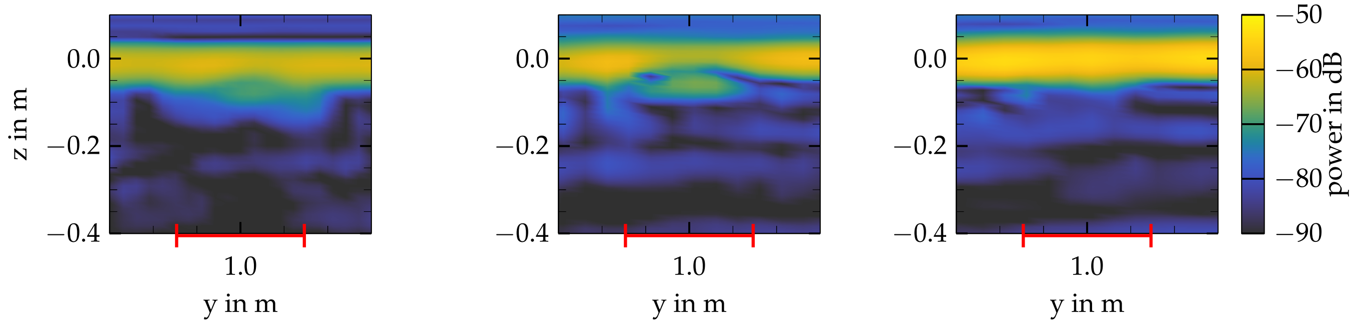

(**a**) $\omega_w = 0.012$ (**b**) $\omega_w = 0.051$ (**c**) $\omega_w = 0.098$

Figure 16. B-Scans at x = 4.00 with different soil moisture content with a shallowly buried aluminum cylinder at (4.00, 1.0, −0.03) (Figure 8a).

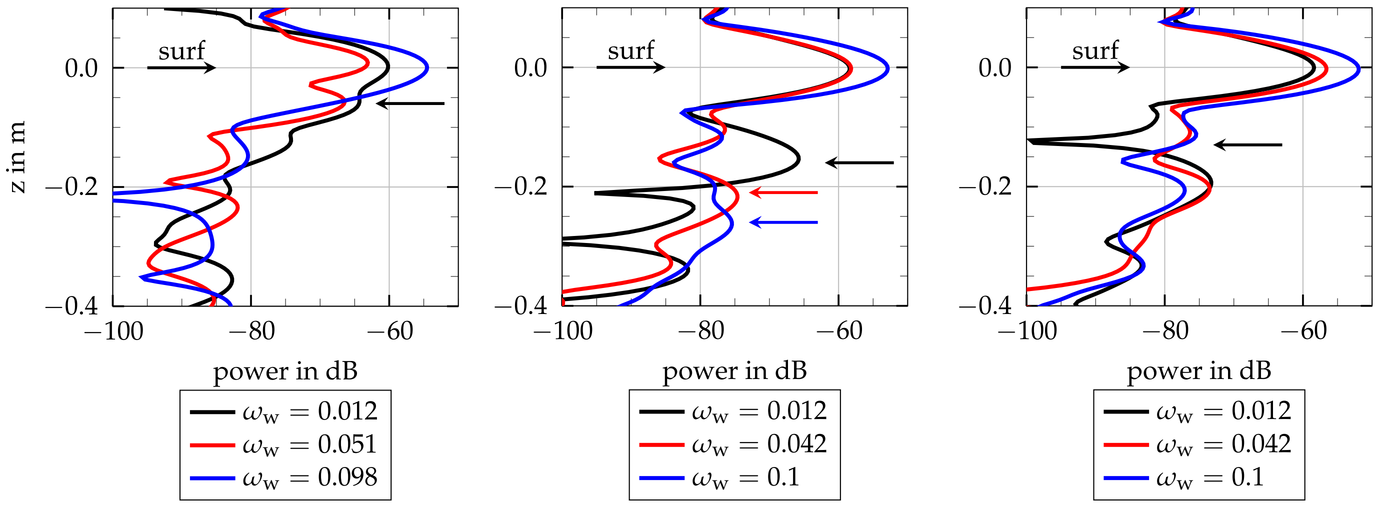

(**a**) Shallowly buried aluminum cylinder (**b**) Aluminum cylinder (**c**) Plastic cylinder

Figure 17. A-Scans from three different objects with different soil moisture content.

Looking at the C-Scans (Figure 18) for two extreme cases—the shallowly buried aluminum cylinder and the plastic cylinder—it is still possible to identify the targets in both cases based on the circular signature, despite the high soil water content. From the known relationship of the expected target phase (Equation (20)) at the correct target range a circular ring pattern with a phase equal to 0 appears, c.f. Figure 18b. However, the case in Figure 18b also implies that under certain circumstances the clutter at the depth of the target has almost the same phase, which can lead to a deterioration in detection capability. The shallowly buried aluminum cylinder is also not visible in the B-Scan or the respective A-Scan. However, in the C-Scan in Figure 18c, a circular shape appears with a relatively high SNR. For this particular measurement, the major problem originates from the limitation that only in a few A-Scans the target response has a high SNR. Therefore, it is possible that in a single B-Scan no visible hyperbola is formed. Thus, it is absolutely necessary to take a B-Scan at the appropriate position above the object in order to detect the target at all. In Figure 18d the corresponding phase of the C-Scan is given and the expected circular 0 phase ring is easily visible and exhibits a phase difference to the background of π. In contrast, the stronger signal in the bottom left corner is easily identifiable as clutter, due to the random phase.

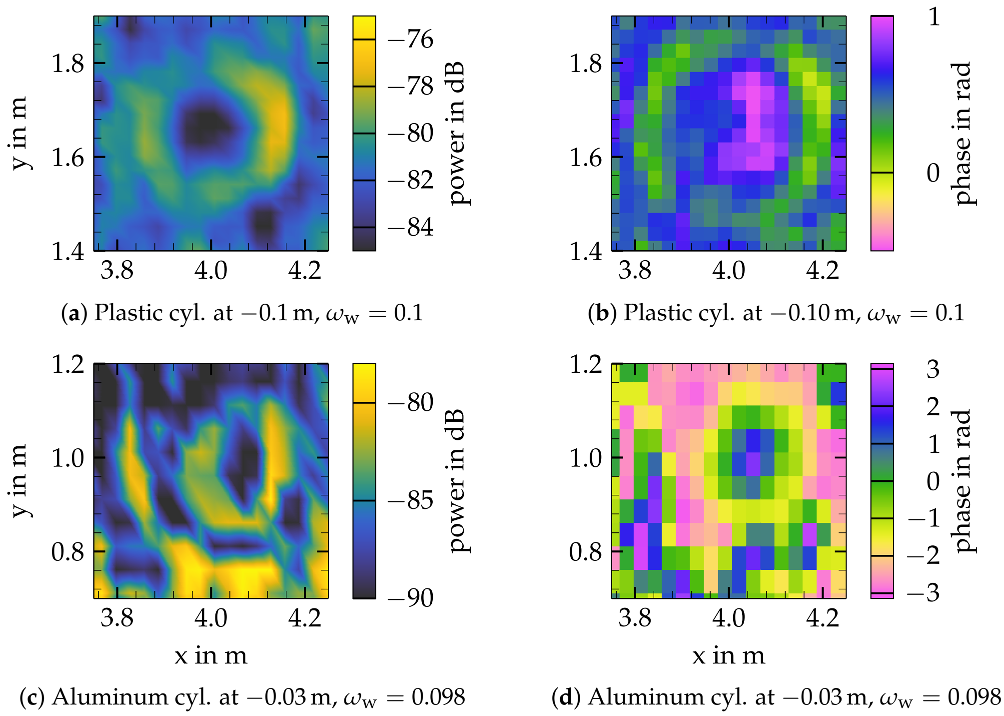

Figure 18. Phase and power C-Scan comparison for two different object for soil with high water content. The respective C-Scan is slightly below the depth corresponding to the real depth.

Conclusions

The measurements principally exhibit the expected behaviour: an increased water content leads into an enhanced surface reflection and simultaneously in an elongation of the path in the medium. This results in a weaker target response for deeper object, whereas the shallowly buried object is hard to perceive especially for the dry soil. Looking at the C-Scans offers a significant improvement. Clear patterns with distinct signatures appear which can be readily identified.

3.2. Surface Roughness

The roughness of the surface is the second important factor influencing the detectability of buried objects. The scattering at the surface increases with enhanced surface roughness. The target response is also frayed, as no more plane waves are received from the object due to multi-path propagation. Therefore, in the following section this influence will be investigated using synthetically generated rough surfaces with the parameters in Table 2.

As a reference, the C-Scan of a smooth surface in Figure 19a is taken. A mean reflected power of 60 dB with a variation of 3 dB from the surface can be determined. This variation can also be seen in the probability density function (pdf) of the bivariate histogram in Figure 20a. Furthermore, a variation in the position of three range bins can be extracted, whereby the majority is limited to two range bins and a power variation of 2 dB. Some of the bins with lower intensity are due to the upper left corner in the C-Scan.

The first investigated surface is surface 1, with parameters listed in Table 2. In the C-Scan in Figure 19b, the periodically repeated pattern of the surface molds is clearly observable in the reflected power, leading to a broader power distribution and larger spreading in the position, c.f. Figure 20b.

Surface 2 as given in Figure 19c, has the highest roughness considered in this work. The same periodicity as for surface 1 can be observed, due to the same orientation of the molds and the identical correlation length ℓ. Only the standard height deviation σ_h is doubled, with respect to surface 1. The power and position deviation spreading is much wider in comparison to the other surfaces. The power is distributed over 13 dB while the position simultaneously varies over 10 range bins, Figure 20c.

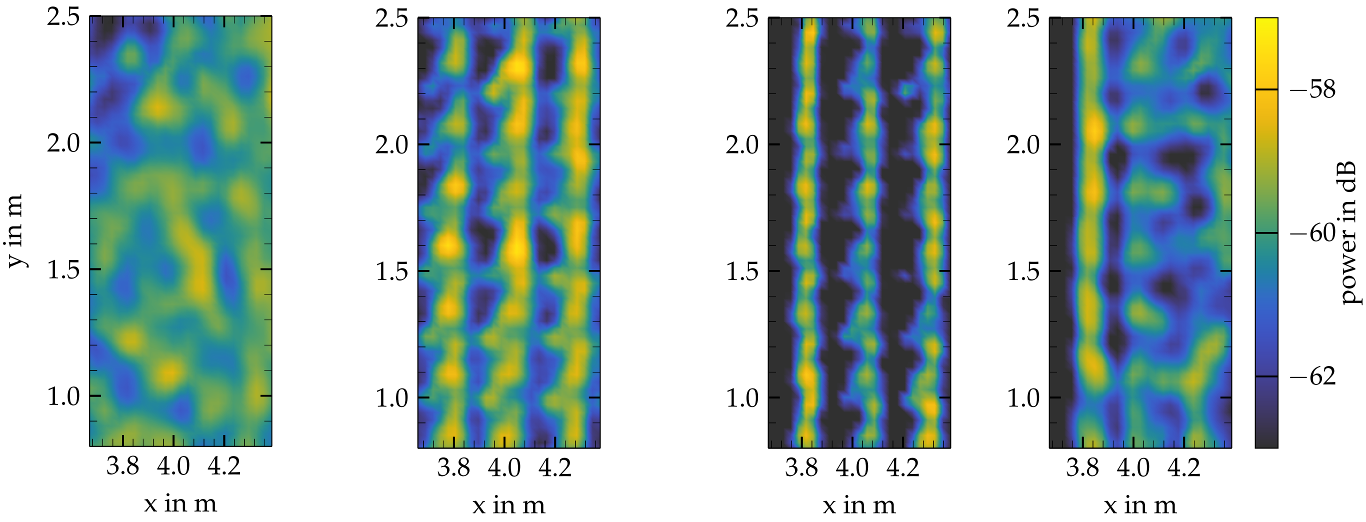

(**a**) plane (**b**) surface 1 (**c**) surface 2 (**d**) surface 3

Figure 19. C-Scans at $\bar{z} = 0$ from four different rough surfaces.

In contrast, surface 3 exhibits a smaller variation due to the smaller correlation length ℓ and σ_h. The major variation in the position ranges over three bins while the spreading of the power is limited to 3 dB.

Based on these observations, a coarse estimation of the correlation between the roughness and the distribution of the range bins can be derived, $6\sigma_h \approx n_{\mathrm{rbins}}\Delta r_{\mathrm{bin}}$. As the relationship between the power distribution and the respective surface parameters is not straightforward, reference is given to the literature [34].

The influence of the surface on the target response is essential for detection. The B-Scan in Figure 21a of the flat surface serves as a reference. All buried aluminum cylinders (at -0.03, -0.1 and -0.2 m) are visible and can be easily detected. Also the shallowly buried aluminum cylinder appears, despite the above-mentioned insufficient range resolution δ_R. Also in the corresponding C-Scans in Figure 22a–c, all objects possess a distinct circular pattern, with a high SNR.

For the wavy surface 1, all three targets are also observable. However, the wavy surface response is not as equally distributed as in the case of the flat surface. The target power of the individual targets is slightly reduced in comparison to the targets buried under the smooth surface. The pattern of the shallowly buried target is slightly disturbed and deformed, additionally the clutter level is increased due to the surface inhomogeneity, while the targets buried at -0.1 and -0.2 m exhibit almost the same pattern as in the case of the smooth surface.

The situation for the roughest surface is totally different, as the shallowly buried object in Figure 22g is only visible due to an area with higher intensity, without a typical pattern. The typical hyperbola is also not present for the shallowly buried aluminum cylinder in the B-Scan in Figure 21c,d. Additionally, the surface power and the shape itself vary significantly, as already discussed. The B-Scan at x = 4.0 m exhibits a surface with a small power spreading. However, below the surface, a periodically repeating clutter area appears, which interacts with the target response of the shallowly buried aluminum cylinder. This behavior is even more pronounced in the B-Scan at x = 4.09 m, as the surface response is reduced by 5 dB to 10 dB in comparison to the B-Scan at x = 4.0 m, and therefore the target disappears. Likewise, the intensity of the deeper buried targets is reduced and no clear pattern is visible in the C-Scans. In contrast, in the B-Scan at x = 4.0 m, the two hyperbolas are clearly distinguishable from the background clutter. If the phase of the

B-Scans Figure 23 is considered, the deeper aluminum cylinders are identifiable due to the hyperbolas with a phase equal to 0. Here, also, the shallowly buried object is detectable, even if the surface structure leads to a periodical pattern with smaller hyperbolas.

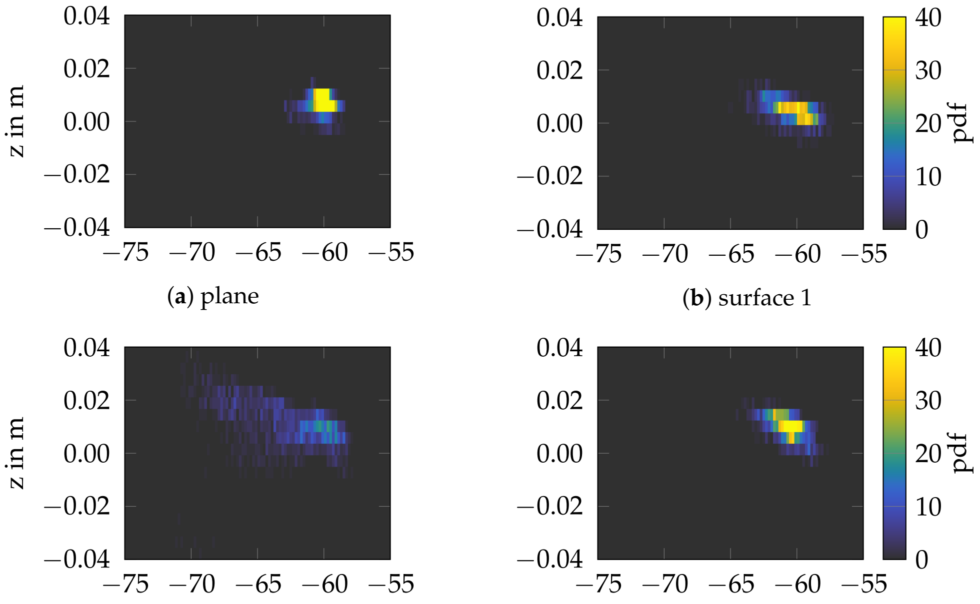

(**a**) plane (**b**) surface 1 (**c**) surface 2 (**d**) surface 3

Figure 20. Bivariate histograms showing the corresponding spreading in position and power for four different rough surfaces, with parameters in Table 2. The spread of the distribution of both variables increases with increasing surface roughness.

Surface 3 is the final surface under investigation with the smallest correlation length ℓ. This leads to a more homogeneous surface response and therefore the circular pattern of the shallowly buried target is visible. Likewise the circular shape of the deeper targets, with a slightly reduced response, are present. In the corresponding B-Scan (Figure 21e) the clutter level directly below the surface peak is reduced and in combination with the slightly reduced surface response, the shallowly buried aluminum cylinder is relatively easy to detect compared to the others. This behavior is also expressed in the SNR (●) in Figure 24.

The SNR shown in Figure 24 represents the ideal case of a homogeneous soil composition with a periodic surface structure. Unfortunately, this assumption does not always apply in the real world, where irregular structures with an inhomogeneous soil composition and the presence of stones and debris occur. As a result, the background clutter increases and the SNR will deteriorate.

However, there are several important observations for the SNR behavior. On one side, the SNR for the deeply buried target changes only slightly over the investigated surfaces. The identical SNR appears for the "wavy" roughness (surface 1), as for the plane surface. Surface 3 with the short correlation length has the lowest SNR due to the increased clutter level at this depth. On the other hand, the aluminum cylinder buried at -0.1 m exhibits the expected behavior: with an increase of the RMS slope ω in combination with the absolute roughness depth and correlation length the SNR decreases. The same behavior is generally observed from the shallowly buried object, with an exception for surface 3. The random coincidence of the target response with an area of low clutter increases the SNR significantly and exceeds that of the smooth surface.

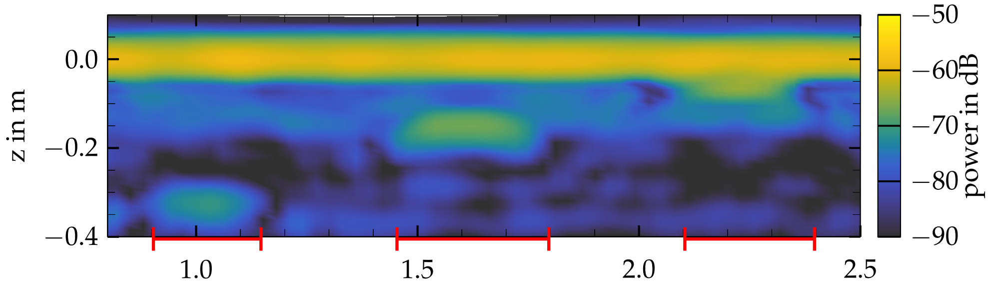

(**a**) plane, x = 4.0 m

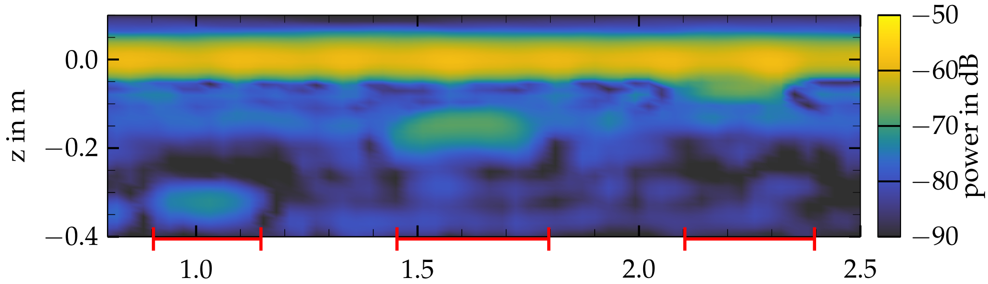

(**b**) surface 1, x = 4.0 m

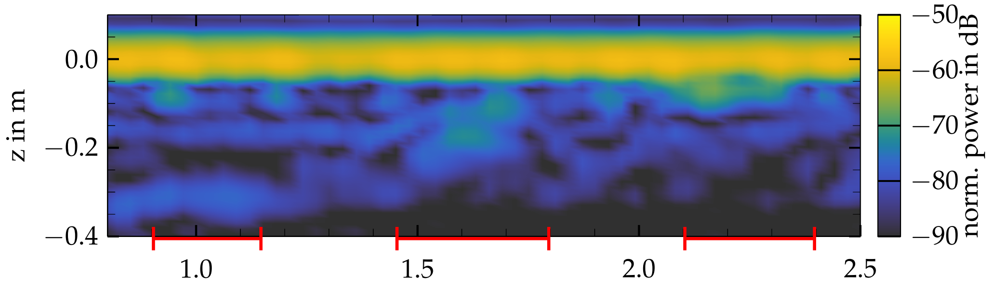

(**c**) surface 2, x = 4.0 m

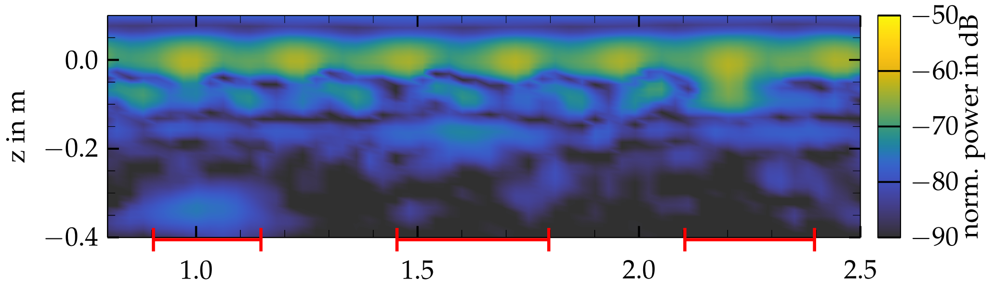

(**d**) surface 2, x = 4.09 m

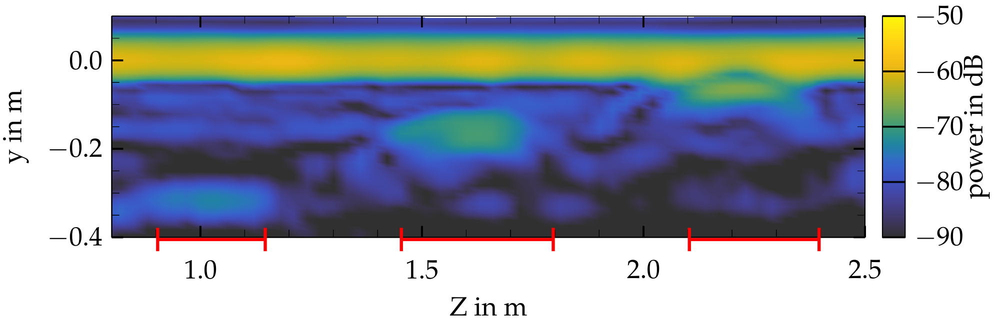

(**e**) surface 3, x = 4.0 m

Figure 21. B-Scans from buried aluminum cylinders (Figure 8a) at (4.0, 1.0, −0.2), (4.0, 1.65, −0.1) and (4.0, 2.25, −0.03) with different surface roughnesses.

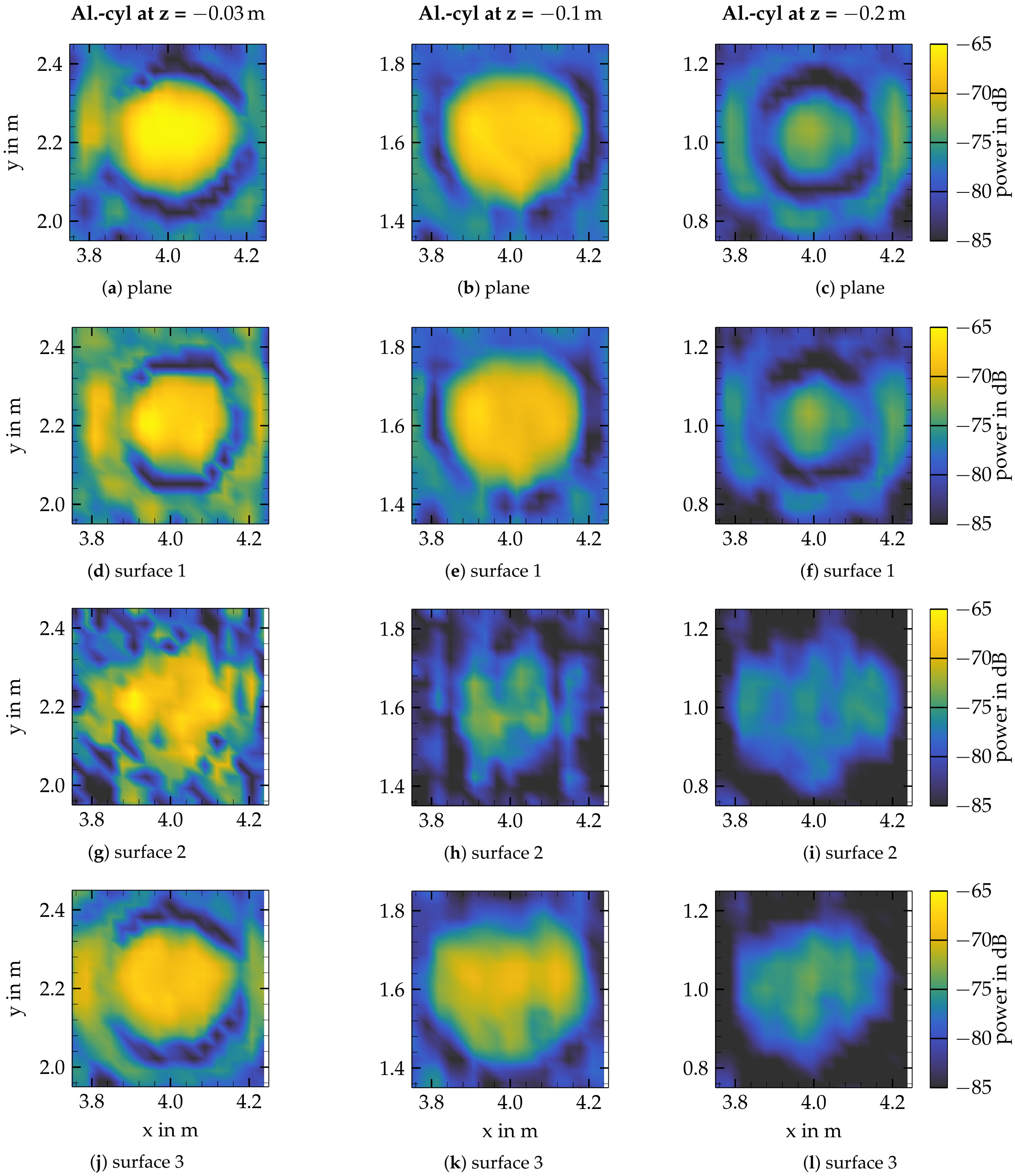

Figure 22. C-Scan comparison of the influence of different burial depths and rough surface parameters on the response of buried aluminum cylinders.

Conclusions

As the surface roughness increases, the impact on the received target response is enhanced. The object pattern, especially of the shallowly buried object, appears frayed and detection becomes more difficult. An improvement can be seen by considering the phase of the B-Scan, which still exhibits clear hyperbolas that contrast significantly from other surface artifacts.

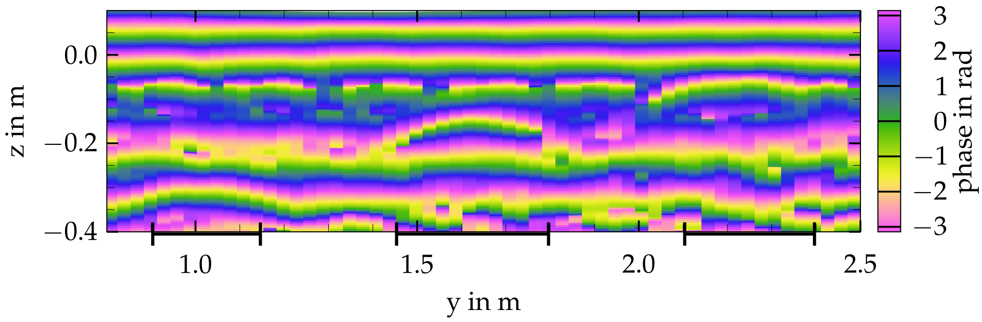

(**a**) x = 4.0 m

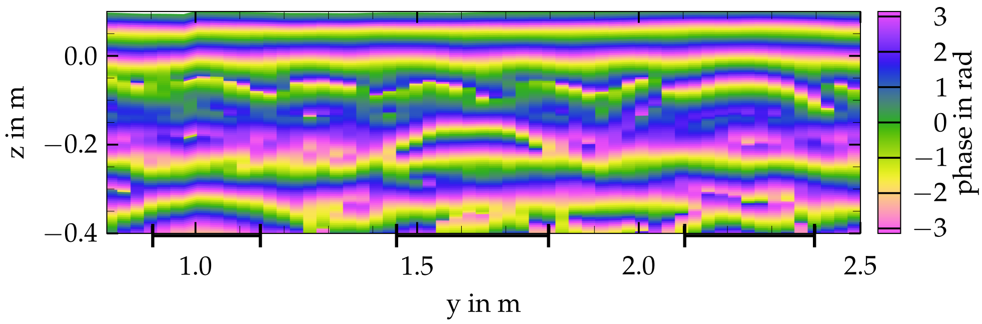

(**b**) x = 4.09 m

Figure 23. Phase of the B-Scan from three buried aluminum cylinders at (4.0, 1.0, −0.2), (4.0, 1.65, −0.1) and (4.0, 2.25, −0.03) (rough surface 2).

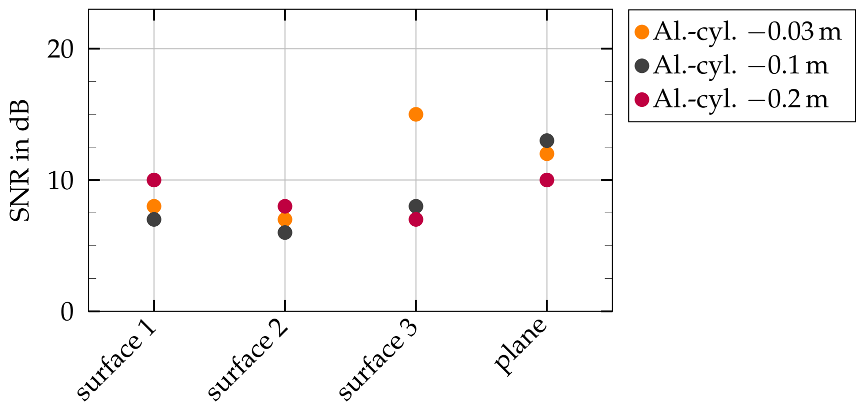

Figure 24. SNR of aluminum cylinders buried in various depths in dry sandy loam with different surface roughnesses.

3.3. Vegetation

Another main influencing factor reflects the local vegetation, as already discussed in theory. An increase in water content leads to stronger reflections from plants. These are also dependent on the structure of the plant in terms of water content, the structure of the stems and the foliage. As a result, the surface reflection and target response is affected by the particular plant species. The experiments presented below involve a plane surface on which grass was seeded and reached a height h_v of 0.1 m, with a vegetation mass of 0.25 $\frac{\mathrm{kg}}{\mathrm{m}^2}$ and a gravimetric water content of 7. Finally a coltsfoot and a thistle were planted to investigate and understand the influence of various vegetation. Due to the watering, the soil had a soil moisture content ω_w of 0.07. In the B-scans, the y-vegetation positions are marked with a ( ) at the top.

The power vs. position histograms exhibit a clear difference compared to the unvegetated flat surfaces in Figure 25a. Based on the correlation of the gravimetric water content with the surface reflection already presented, it should result in a reflected mean power of -56 dB, c.f. Figure 12. The mean reflected power is around -60 dB at the surface ($\bar{z} = 0.01$ m) shown in Figure 25b. The spreading of the position and of the reflected power is much wider as compared to the unvegetated surface. Also some slightly weaker reflections occur above the main surface reflection. This leads to the assumption that the electromagnetic waves are scattered by the vegetation. This behavior is intensified by the coltsfoot and thistle for the monostatic antenna arrangement as implied by the histogram in Figure 25c. A larger spreading of both parameters occurs with no main scattering power and no dominant position.

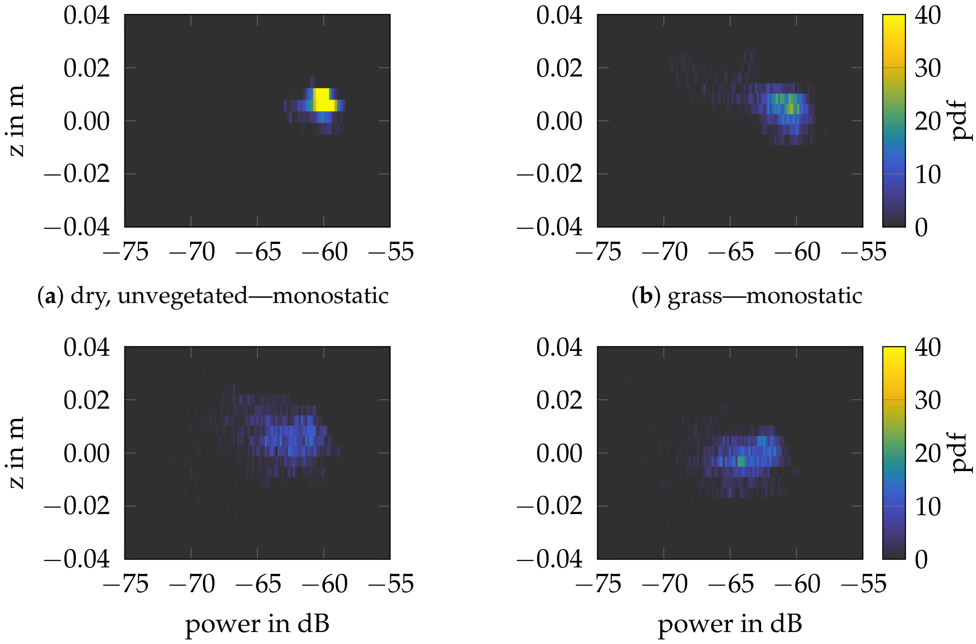

(**a**) dry, unvegetated—monostatic (**b**) grass—monostatic

(**c**) grass and plants—monostatic (**d**) grass and plants—bistatic

Figure 25. Histograms of a plane surface with vegetation.

The identical scenario is presented for a bistatic antenna arrangement in Figure 25d. Due to the bistatic arrangement the spreading in both directions is reduced and the center of gravity exhibits a slightly reduced reflected power and appears slightly deeper.

Comparing the B-Scans in Figure 26 in detail, the influence of the coltsfoot, c.f. Figure 10c, at x = 2.0 m is immediately apparent. The coltsfoot with its areal root system and many individual stems with plate-like leaves, leads to a scattering volume, with a few small target like hyperbolas. The same behavior is clearly visible in the phase of the B-Scan in Figure 27a. Here, the plant leads to a disturbed clutter above the surface, with a 0 phase pattern. The surface reflection below the plant is also reduced due to the scattering within the plant. Compared to the bistatic arrangement, the reduced surface reflection is clearly observable in the B-Scan. Additionally, there are no strong reflections from the plant that can be interpreted as ghost targets.

Considering the signal response of the buried aluminum cylinders, the shallow one can be easily detected due to the small influence of the uniformly grown grass. On the other hand, for the deeper aluminum cylinder in the monostatic case, the target pattern is recognizable in the B-Scan, especially due to the occurrence of a hyperbola with a negative contrast. This object is no longer visible in the monostatic power B-Scan, when a plant, in this case the coltsfoot, grows in the immediate vicinity above the target. The same applies to the bistatic power B-Scan. If, additionally, the corresponding phase of the B-Scans is considered, small, barely recognizable 0 phase hyperbolas occur for the monostatic case. For the bistatic arrangement, the two-phase hyperbolas of the targets are easily recognizable.

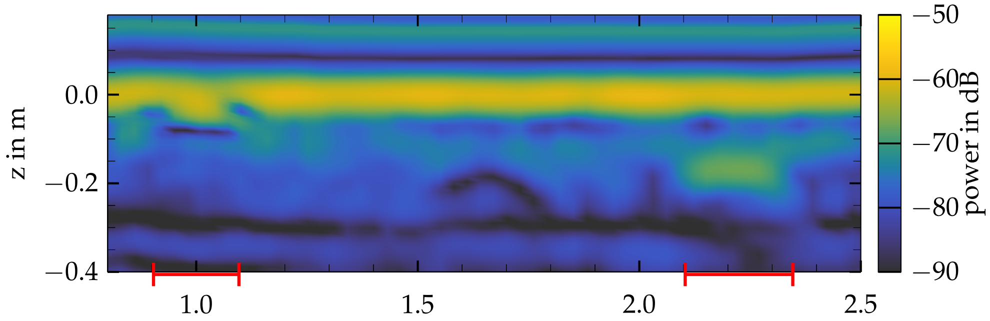

(**a**) plane—monostatic

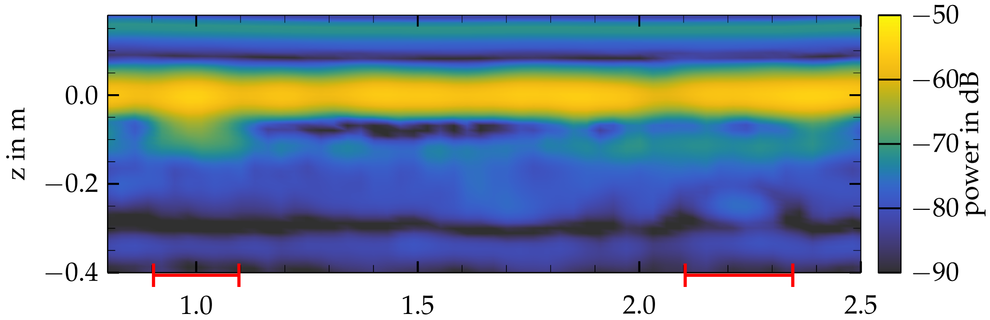

(**b**) grass—monostatic

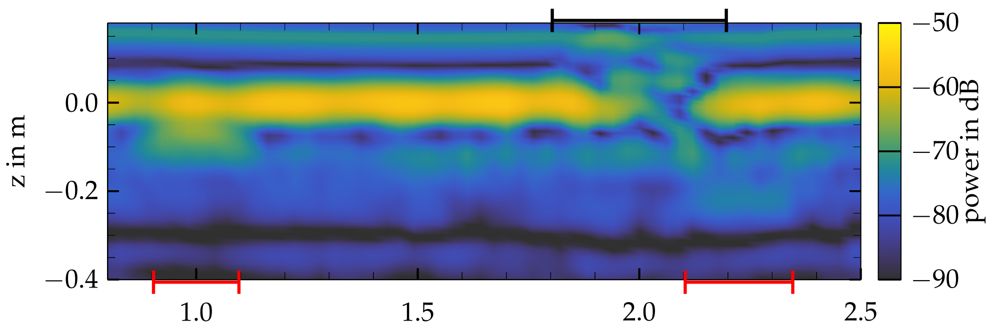

(**c**) grass and coltsfoot—monostatic

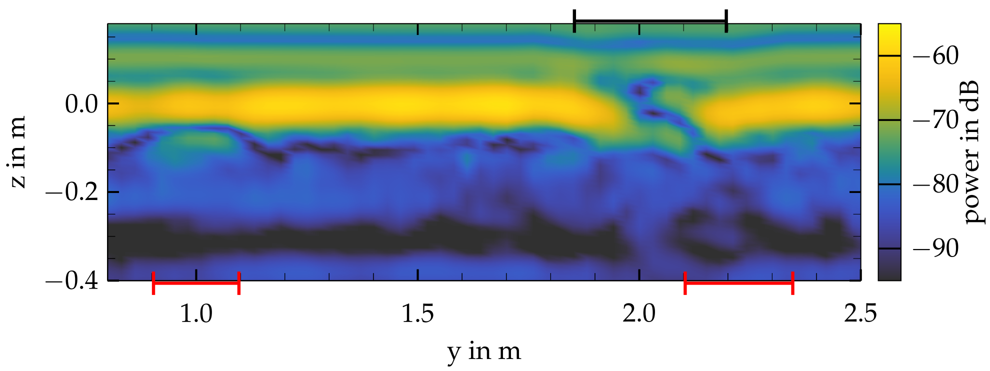

(**d**) grass and coltsfoot—bistatic

Figure 26. B-Scans from aluminum cylinders buried at (4.0, 1.05, −0.03) and (4.0, 2.2, −0.1) with growing vegetation at (4.0, 2.05, 0.1).

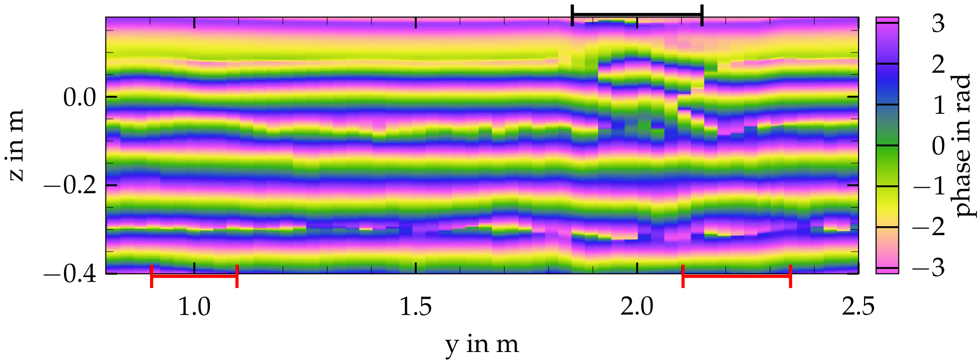

(**a**) monostatic

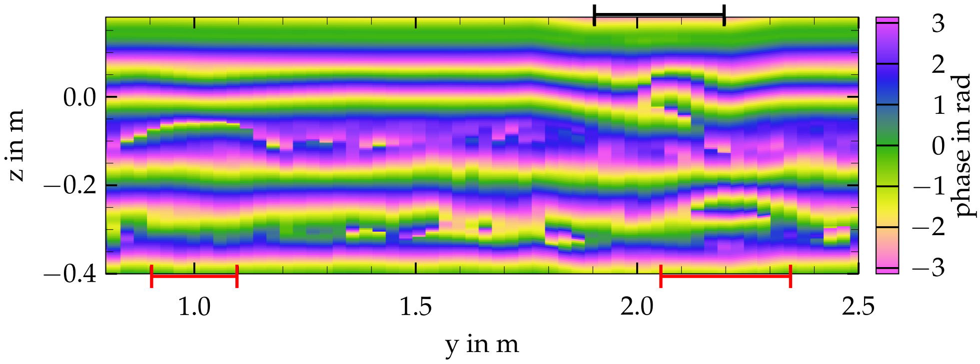

(**b**) bistatic

Figure 27. Phase of the B-Scan from aluminum cylinders buried at (4.0, 1.05, −0.03) and (4.0, 2.2, −0.1) with vegetation of grass and coltsfoot at (4.0, 2.05, 0.1).

Conclusions

The evenly distributed grass scatters the electromagnetic waves, reducing the surface reflection. The shallowly buried object remains visible and can be detected. Plants with individual strong stems that contain water, on the other hand, result in significant scattering. As a result, these plants can be eventually interpreted as targets and the objects below are no longer detectable in the intensity B-Scan. An improvement can be achieved by looking at the bistatic phase of the B-Scan.

3.4. Comparison of the Various Influences

For each of the investigated scenarios certain parameters impose challenges for the detection of buried targets. An increase of the ε_r' due to the water content is responsible for a change in the measured target depth. Also, the reflected power at the surface increases, leading to a reduction in transmission, further enhanced by the increase of the ε_r''. Due to the homogeneity of the soil moisture prevailing in the tests, nevertheless it is possible to identify the specific target pattern up to a gravimetric water content of 0.1.

The surface roughness generally leads to a deterioration of the target response and blurs the specific target pattern. This is especially true for shallowly buried objects in combination with a high surface roughness. Similar results were obtained for the vegetation: the shallowly buried object is detectable for an uniform distribution of grass. If the structure of the plants changes with respect to the shape of the foliage and the stems with a simultaneous increase of the water content (coltsfoot), the impact increases considerably and significantly worsening the detection capability, especially of the shallowly buried objects. The clearest appearance of deeply buried objects in the presence of plants could be observed for the phase of the B-Scan in a bistatic setup.

4. Discussion and Conclusions

In this contribution challenges and concepts for a GPR-based detection of buried objects, especially for landmines, are presented and discussed. A major issue related to field measurements is the radar response to vegetation and soil properties leading to undetected objects with respect to the ground truth (false negatives) but also to false alarms (false positives). Our approach can be characterized by the following items:

- Separation and quantification of environmental impact parameters;
- Identification of critical paths for landmine detection;
- Optimization of data representation for a robust detection.

4.1. Separation of Environmental Impact Parameters

A major challenge for the interpretation of field measurements, specifically with respect to the impact of soil properties, surface topography and vegetation, is the lack of a well-characterized and defined measurement environment resulting in an only qualitative correlation between detection robustness and environment parameters. In our approach, we separated the impact of soil moisture, surface roughness and vegetation, however, using the identical radar setup. By watering the surface of our loamy sand in several steps and measuring the gravimetric water content prior to and after each measurement, the obtained GPR data could be correlated accurately to the moisture. Based on our molding technique we could generate a surface topography defined by the lateral correlation lengths, rms-roughness and the resulting slopes. Growing grass on the surface and planting single plants, the impact of an homogeneous or inhomogeneous vegetation could be analyzed. Another important aspect is the generation of regular reading points based on an equidistant grid which is essential for the appearance of signatures for buried objects.

4.2. Identification of Critical Paths for Landmine Detection

An enhanced moisture content in the soil affects surface reflections and the attenuation of electromagnetic waves in the soil. Through an enhanced attenuation the detection depth can be significantly reduced. This issue is reinforced by a reduced surface penetration of radar waves as a consequence of an augmented surface reflectivity. An eventually even more limiting factor arises for shallow objects such as APMs. Due to the radar bandwidth and a resulting limited range resolution, a strong surface reflection cannot be separated from the shallow object. With respect to the surface roughness, only the "roughest" surface deteriorated the GPR-data to a significant degree, blurring the pattern and signatures of buried objects (Figure 22). Again, shallow objects are affected to a larger amount, as it becomes more and more difficult to distinguish blurred patterns of relevant objects from similar patterns from a rough and heterogeneous surface topology. With respect to vegetation, a homogeneous natural vegetal cover with green grass could not deteriorate the detection of buried objects tremendously. However, the implanting of plants with an irregular leaf and root structure affected the detection of buried objects by locally enhanced scattering and shading of the area under these plants. Such "heterogeneities" especially enhance the rate of false alarms as it appears hard to distinguish relevant objects from these plants.

4.3. Optimization of Data Representation for a Robust Detection

Despite these issues and challenges, all buried objects (even the plastic cylinders in combination with the largest moisture content) could be observed and recognized from the radar data! A key issue is the observation of distinct patterns and signatures which, however, appear only for certain data representations and images. These signatures include hyperbolas, circles and rings which, of course, only become apparent for 2D cross sectional images (vertical—B-Scan, horizontal—C-Scan). Single vertical distance scans (A-Scan) cannot reflect such signatures, limiting this data representation to rather "easy" environments. The interference of reflections from objects with clutter or the surface can even improve the visibility of the above described signatures by the formation of "dark" hyperbolas or rings resulting in a higher contrast within the corresponding radar images. A major outcome of this work is the importance of phase images. In these phase images, certain patterns (e.g., hyperbolas) are clearly visible whereas in the intensity image the corresponding signature cannot be distinguished from a heterogeneous background clutter or from strong surface reflections (compare Figure 26d and Figure 27b). However, there is no general recipe how to represent GPR data for a robust and reliable detection of buried landmines under different environmental impacts. We could see all buried objects. However, it appears to be essential that a data representation is selected exhibiting these typical signatures with a sufficient contrast. A final remark addresses the issue of false alarms, pointing out that the combination of different radar images can result in a high detection rate and reduce false alarms. In the phase image of Figure 27b, the hyperbolas of two buried objects appear clearly. However, at the position of the coltsfoot another hyperbola can be seen making it difficult to judge if another relevant object is present. Looking at the corresponding intensity B-Scan (Figure 26d), only one buried object becomes apparent. Nevertheless, at the position of the coltsfoot the surface appears distorted and disturbed, implying a high local scattering which is typical for such kind of plants. Thus, the proposed combination of data facilitates the classification of detections leading to a high detection rate of relevant objects in combination with moderate false alarm rates.

Author Contributions: Formal analysis, B.A.; Methodology, B.A.; Project administration, W.M.; Supervision, T.W.; Visualization, B.A.; Writing—original draft, B.A.; Writing—review and editing, M.S. All authors have read and agreed to the published version of the manuscript.

Funding: This research was funded by the URS ENDRESS Foundation (https://www.ue-stiftung.org/, accessed on 31 January 2024) under the project FindMine (https://www.findmine.org/, accessed on 31 January 2024).

Data Availability Statement: Data are contained within the article.

Conflicts of Interest: Author Winfried Mayer was employed by the company FindMine gGmbH. The remaining authors declare that the research was conducted in the absence of any commercial or financial relationships that could be construed as a potential conflict of interest.

References

1. Sherwin, M. *Landmine Monitor 2022: Landmine Monitor 24th Annual Edition*; Landmine and Cluster Munition Monitor ICBL-CMC: Geneva, Switzerland, 2022; ISBN 978-2-9701476-2-6. Available online: https://www.the-monitor.org/en-gb/reports/2022/landmine-monitor-2022.aspx (accessed on 15 January 2024).
2. Schartel, M.; Burr, R.; Bähnemann, R.; Mayer, W.; Waldschmidt, C. An Experimental Study on Airborne Landmine Detection Using a Circular Synthetic Aperture Radar. *arXiv* **2020**, arXiv:2005.02600.
3. García-Fernández, M.; Álvarez Narciandi, G.; Álvarez López, Y.; Las-Heras, F. Array-Based Ground Penetrating Synthetic Aperture Radar on Board an Unmanned Aerial Vehicle for Enhanced Buried Threats Detection. *IEEE Trans. Geosci. Remote Sens.* **2023**, *61*, 5104218. [CrossRef]
4. Garcia-Fernandez, M.; Alvarez-Narciandi, G.; Lopez, Y.A.; Andres, F.L.H. SAFEDRONE project: Development of a UAV-based high-resolution GPR system for IED detection. In Proceedings of the 2022 16th European Conference on Antennas and Propagation (EuCAP), Madrid, Spain, 27 March–1 April 2022. [CrossRef]
5. Kondo, T.; Kikuta, K.; Sato, M. Ground Surface Reflection Compensation for Hand-Held GPR. *IEEE Geosci. Remote Sens. Lett.* **2022**, *19*, 3501605. [CrossRef]
6. Vallon. *Vallon VMR3G Minehound-Dual-Sensor-Detektor*; Vallon GmbH: Eningen, Germany, 2024. Available online: https://vallon-dual-sensor-detectors.com/de/ (accessed on 5 January 2024).
7. Romero, I.; Walter, T.; Mariager, S. Wavelet Transform Analysis for a Continuous Wave Metal Detector for UAV Applications. In Proceedings of the IGARSS 2023—2023 IEEE International Geoscience and Remote Sensing Symposium, Pasadena, CA, USA, 16–21 July 2023. [CrossRef]
8. García-Fernández, M.; López, Y.A.; Andrés, F.L.H. Airborne Multi-Channel Ground Penetrating Radar for Improvised Explosive Devices and Landmine Detection. *IEEE Access* **2020**, *8*, 165927–165943. [CrossRef]
9. Grathwohl, A.; Arendt, B.; Grebner, T.; Waldschmidt, C. Detection of Objects Below Uneven Surfaces With a UAV-Based GPSAR. *IEEE Trans. Geosci. Remote Sens.* **2023**, *61*, 5207913. [CrossRef]
10. Debye, P.J.W. *Polar Molecules*; The Chemical Catalog Company, Inc.: New York, NY, USA, 1929.
11. Said, T.; Varadan, V.V. Variation of Cole-Cole model parameters with the complex permittivity of biological tissues. In Proceedings of the 2009 IEEE MTT-S International Microwave Symposium Digest, Boston, MA, USA, 7–12 June 2009. [CrossRef]

12. Bobrov, P.P.; Kroshka, E.S.; Lapina, A.S.; Repin, A.V. Relaxation model of complex relative permittivity of sandstones for the frequency range from 10 kHz to 1 GHz. In Proceedings of the 2017 Progress In Electromagnetics Research Symposium—Spring (PIERS), St. Petersburg, Russia, 22–25 May 2017. [CrossRef]
13. Peplinski, N.; Ulaby, F.; Dobson, M. Dielectric properties of soils in the 0.3–1.3-GHz range. *IEEE Trans. Geosci. Remote Sens.* **1995**, *33*, 803–807. [CrossRef]
14. Topp, G.C.; Davis, J.L.; Annan, A.P. Electromagnetic determination of soil water content: Measurements in coaxial transmission lines. *Water Resour. Res.* **1980**, *16*, 574–582. [CrossRef]
15. Scharf, P.A.; Iberle, J.; Mantz, H.; Walter, T.; Waldschmidt, C. Multiband Microwave Sensing for Surface Roughness Classification. In Proceedings of the 2018 IEEE/MTT-S International Microwave Symposium–IMS, Philadelphia, PA, USA, 10–15 June 2018. [CrossRef]
16. Tan, H.S. Microwave measurements and modelling of the permittivity of tropical vegetation samples. *Appl. Phys.* **1981**, *25*, 351–355. [CrossRef]
17. Mahmoudzadeh Ardekani, M.R.; Jacques, D.C.; Lambot, S. A Layered Vegetation Model for GPR Full-Wave Inversion. *IEEE J. Sel. Top. Appl. Earth Obs. Remote Sens.* **2016**, *9*, 18–28. [CrossRef]
18. Wehner, D.R. *High Resolution Radar*, 2nd ed.; Artech House Radar Library, Artech House: Norwood, MA, USA, 1995.
19. Davis, J.L.; Annan, A.P. Ground-Penetrating Radar for high-resolution mapping of soil and rock stratigraphy. *Geophys. Prospect.* **1989**, *37*, 531–551. [CrossRef]
20. Turk, A.S. *Subsurface Sensing*, 1st ed.; Wiley Series in Microwave and Optical Engineering Ser; John Wiley & Sons Incorporated: Hoboken, NJ, USA, 2011; Volume 197.
21. Warren, C.; Giannopoulos, A.; Giannakis, I. gprMax: Open source software to simulate electromagnetic wave propagation for Ground Penetrating Radar. *Comput. Phys. Commun.* **2016**, *209*, 163–170. [CrossRef]
22. Perdok, U.; Kroesbergen, B.; Hilhorst, M. Influence of gravimetric water content and bulk density on the dielectric properties of soil. *Eur. J. Soil Sci.* **1996**, *47*, 367–371. [CrossRef]
23. Roth, K.; Schulin, R.; Flühler, H.; Attinger, W. Calibration of time domain reflectometry for water content measurement using a composite dielectric approach. *Water Resour. Res.* **1990**, *26*, 2267–2273. [CrossRef]
24. Arendt, B.; Grathwohl, A.; Waldschmidt, C.; Walter, T. Influence of Vegetation on the Detection of Shallowly Buried Objects with a UAV-Based GPSAR. In Proceedings of the IGARSS 2022—2022 IEEE International Geoscience and Remote Sensing Symposium, Kuala Lumpur, Malaysia, 17–22 July 2022. [CrossRef]
25. Geng, N.; Wiesbeck, W. *Planungsmethoden für die Mobilkommunikation*; 1., softcover reprint of the original 1st ed. 1998 ed.; Information und Kommunikation; Springer: Berlin, Germany, 2013.
26. Thomas, T.R. *Rough Surfaces*; Published by Imperial College Press and Distributed by World Scientific Publishing Co.: London, UK, 1998. [CrossRef]
27. Bergström, D.; Powell, J.; Kaplan, A.F. The absorption of light by rough metal surfaces—A three-dimensional ray-tracing analysis. *J. Appl. Phys.* **2008**, *103*, 103515. [CrossRef]
28. Tsang, L.; Kong, J.A.; Ding, K. *Scattering of Electromagnetic Waves: Theories and Applications*; Wiley: New York, NY, USA, 2000. [CrossRef]
29. Keysight. *Network Analyzer FieldFox Handheld RF*; Keysight: Santa Rosa, CA, USA, 2023. Available online: https://www.keysight.com/us/en/products/network-analyzers/fieldfox-handheld-rf-microwave-analyzers.html (accessed on 8 January 2024).
30. Aaronia. *AARONIA PowerLOG® 70180 Hornantenna*; Aaronia AG: Euscheid, Germany, 2023. Available online: https://aaronia.com/de/shop/antennen-sensoren/horn-antennas/horn-antenna (accessed on 20 January 2024).
31. Harris, F. On the use of windows for harmonic analysis with the discrete Fourier transform. *Proc. IEEE* **1978**, *66*, 51–83. [CrossRef]
32. Adams, J. A new optimal window (signal processing). *IEEE Trans. Signal Process.* **1991**, *39*, 1753–1769. [CrossRef]
33. Yelf, R. Where is true time zero? In Proceedings of the Tenth International Conference on Ground Penetrating Radar, Delft, The Netherlands, 21–24 June 2004; GPR 2004; Univ. of Technology: Delft, The Netherlands, 2004.
34. Ulaby, F.T.; Moore, R.K.; Fung, A.K. *Radar Remote Sensing and Surface Scattering and Emission Theory*; Artech House: Norwood, MA, USA, 1986; Volume 2.